ACS Catalysis

pubs.acs.org/acscatalysis Research Article

Coenzyme Engineering of Glucose-6-phosphate Dehydrogenase on a Nicotinamide-Based Biomimic and Its Application as a Glucose Biosensor

Dongdong Meng,[#] Meixia Liu,[#] Hao Su,[*] Haiyan Song, Lijie Chen, Qiangzi Li, Ya-nan Liu, Zhiguang Zhu, Weidong Liu, Xiang Sheng, Chun You,[*] and Yi-Heng P. Job Zhang

Cite This: *ACS Catal.* 2023, 13, 1983−1998 Read Online

ACCESS | Metrics & More | Article Recommendations | Supporting Information

ABSTRACT: Nicotinamide adenine dinucleotide (NAD(P)$^+$)-dependent oxidoreductases have been widely employed as biocatalysts for numerous applications, such as *in vitro* biomanufacturing and biosensors. The application of biomimetic nicotinamide coenzymes (BNCs) in an enzymatic redox cascade constitutes a promising alternative that can eliminate the need for expensive natural NAD(P)$^+$ coenzymes. Herein, we demonstrated that the coenzyme engineering of glucose-6-phosphate dehydrogenase from *Zymomonas mobilis* (ZmG6PDH) enhanced its catalytic efficiency (k_{cat}/K_m) on oxidized nicotinamide mononucleotide (NMN$^+$). Compared with the wild-type (WT) enzyme, the optimal mutant R4 exhibited a 112-fold enhancement in catalytic efficiency on NMN$^+$, with 4.7 × 10^3 and 2.6 × 10^3-fold change in the two coenzyme specificity values ($[k_{cat}/K_m]_{NMN}{}^+/[k_{cat}/K_m]_{NAD}{}^+$ and $[k_{cat}/K_m]_{NMN}{}^+/[k_{cat}/K_m]_{NADP}{}^+$), respectively. To obtain insights into the structure−function relationship of the enzyme and its mutant, we determined the crystal structures of WT G6PDH (apo-WT) and the complex of mutant R4 and NMN$^+$ (R4:NMN$^+$) and performed molecular dynamics simulations of the ternary complexes of the G6PDH/substrate (glucose-6-phosphate, G6P)/coenzyme. The results revealed that the helix region of the coenzyme-binding Rossmann-like domain in mutant R4 was nearer to the active site than the wild-type enzyme, thus creating a more compact substrate/coenzyme-binding site to favor the binding of the substrate G6P and NMN$^+$. Furthermore, a glucose biosensor based on the glucokinase (GK)/G6PDH-NMN$^+$ biosystem without cryopreservation was constructed using NMN$^+$ as the coenzyme. These results indicate that the combination of BNCs and oxidoreductases can be widely employed in biosensors, biocatalysis, and *in vitro* biomanufacturing.

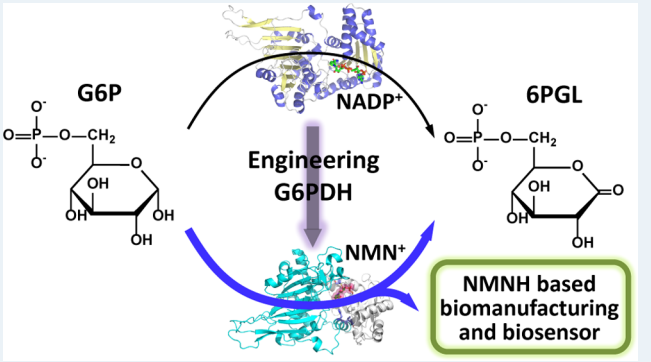

KEYWORDS: *oxidoreductase, biomimetic nicotinamide coenzyme, nicotinamide mononucleotide, glucose-6-phosphate dehydrogenase, biosensor*

INTRODUCTION

Enzymes are exceptionally efficient catalysts that can accelerate chemical reactions with high chemoselectivity, regioselectivity, and stereoselectivity.[1] Along with the development of enzymatic technologies, there has emerged a trend of synthesizing organic compounds via enzymes; for example, using oxidoreductases for biomanufacturing high-value chemicals.[2−4] Nicotinamide-based coenzymes, such as nicotinamide adenine dinucleotide (NAD$^+$/NADH) and nicotinamide adenine dinucleotide phosphate (NADP$^+$/NADPH), are essential for approximately two-thirds of oxidoreductases in redox reactions.[5] However, the NAD$^+$/NADP$^+$-based biotransformation faces economic challenges alongside problems with stability and coenzyme regeneration, which constitute the major bottlenecks for *in vitro* biomanufacturing of low- and medium-cost products.[6] Substituting natural nicotinamide coenzymes in *in vitro* enzyme catalysis with biomimetic nicotinamide coenzymes (BNCs) is a promising approach for solving such concerns.[4,6,7] Compared with natural coenzymes comprising nicotinamide (responsible for hydride transfer) and adenosine dinucleotide (responsible for coenzyme recognition and localization) moieties,[4] BNCs typically retain only the essential nicotinamide moiety, whereas the rest are substituted by chemically stable fragments, including those of sugar, phenyl, and benzyl, to form oxidized nicotinamide flucytosine

Received: September 24, 2022
Revised: January 7, 2023

https://doi.org/10.1021/acscatal.2c04707
ACS Catal. 2023, 13, 1983−1998

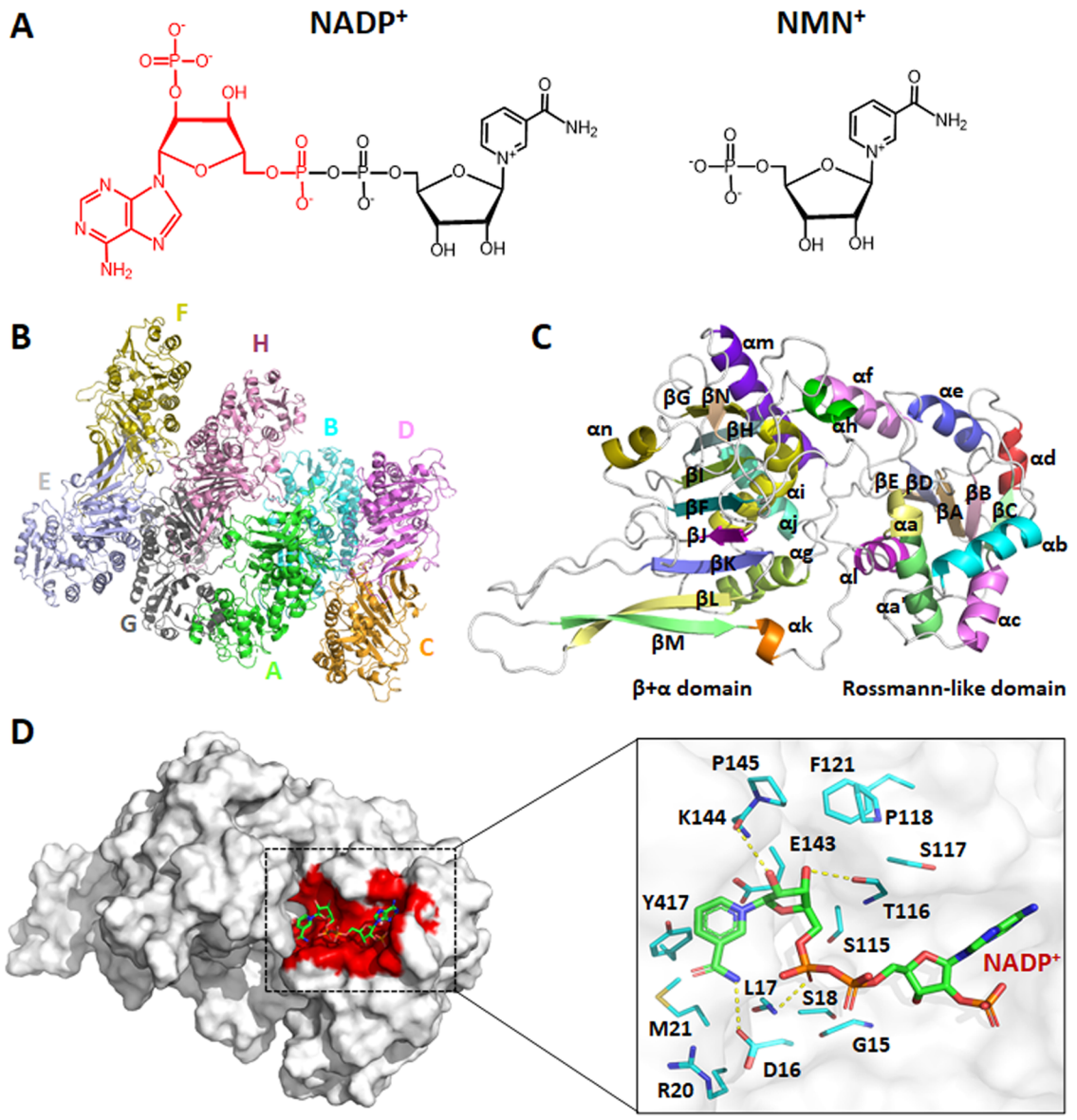

Figure 1. (A) Chemical structures of NADP$^+$ and NMN$^+$. (B) The crystal structures of apo-WT of ZmG6PDH, the eight monomers in one asymmetry unit of apo-WT. (C) The overall structure of wild-type ZmG6PDH, which was the molecule F in the asymmetry unit of apo-WT. The core structure of G6PDH comprises Rossmann-like and β+α domains. (D) Fifteen residues were adjacently located (<5.0 Å) to the NMN$^+$ portion of NADP$^+$ in wild-type ZmG6PDH. Yellow dashed lines indicate the hydrogen bonds.

dinucleotide (NFCD$^+$), nicotinamide mononucleotide (NMN$^+$), nicotinamide riboside (NR$^+$), 1-benzyl nicotinamide (BNA$^+$), etc.[5] Of these, NMN$^+$ (Figure 1A) exhibits higher atom economy and thermostability than NAD(P)$^+$, with a half-life approximately twice as long as that of NAD(P)$^+$ at 60 °C.[8] The strategy of using BNCs as the coenzymes can potentially decrease the processing cost of oxidoreductase-catalyzed biotransformation. However, efficient utilization of BNCs by oxidoreductases constitutes the major obstacle to their biocatalytic application of BNCs.[6,7,9]

Numerous natural enzymes, such as old yellow enzymes,[10−12] diaphorase,[13] nitroreductase,[14,15] monooxygenase,[16] and NADH oxidase,[17] have been reportedly utilized to reduce BNCs in reduction reactions. However, all of them possess a prosthetic group containing flavin adenine dinucleotide (FAD) that nonselectively facilitates electron transfer. For example, in the old yellow enzyme OYE3 isolated from *Saccharomyces pastorianus*, reduced N-benzyl nicotinamide (BNAH) exhibits a considerably higher catalytic efficiency as a coenzyme than NADH.[10] However, the regeneration of reduced BNC is difficult owing to their altered redox potentials, structural differences with natural coenzymes, and improper positioning in the catalytic center of oxidoreductases.[6,18,19] The catalytic efficiency values of numerous wild-type (WT) oxidoreductases (such as alcohol dehydrogenase from *Pyrococcus furiosus* and glucose dehydrogenase from *Sulfolobus solfataricus*) on BNCs were orders of magnitude lower than the values of those on natural cofactors.[20,21] Nevertheless, several enzymes have been engineered for the *in situ* regeneration of reduced BNCs,[8,20−22] thereby establishing the foundation of their application in enzymatic reactions. For example, engineering a coenzyme-binding site of glucose dehydrogenase (SsGDH) from *S. solfataricus* increased the catalytic number (k_{cat}) value of a mutant with two mutation

https://doi.org/10.1021/acscatal.2c04707
ACS Catal. 2023, 13, 1983−1998

sites on BNA$^+$ by 5.6 times.[21] Similarly, an alcohol dehydrogenase mutant exhibiting broadened coenzyme specificity has been used in NMN$^+$-dependent enzymatic biofuel cells.[20] Black et al. used computational approaches to show the switching of the coenzyme specificity from NADP$^+$ to NMN$^+$ in glucose dehydrogenase from *Bacillus subtilis*.[22] Several high-throughput screening methods have highlighted the possibility and validated the generation of BNC-active dehydrogenases. For example, Huang et al. developed a NAD(P)$^+$-eliminated solid-phase assay (NESPA) to identify NMN$^+$-active glucose-6-phosphate dehydrogenase (G6PDH, EC 1.1.1.49) and 6-phosphogluconate dehydrogenase (6PGDH, EC 1.1.1.44) from *Thermotoga maritima*.[8] Furthermore, Zachos et al. employed a photometric-based microfluidic screening system to evolve carba-NADP$^+$-preferred SsGDH.[23]

G6PDH and 6PGDH constitute the key enzymes in the pentose phosphate pathway that catalyzes the regeneration of NADPH. Two moles of NAD(P)H are produced from one mole of glucose-6-phosphate (G6P) via cascade reactions catalyzed by G6PDH and 6PGDH. As an alternative to the expensive G6P substrate, several *in vitro* synthetic enzymatic biosystems have been constructed to use inexpensive materials, such as starch, cellulose, sucrose, and glucose, as substrates to produce G6P, thereby facilitating the biomanufacturing of hydrogen, bioelectricity, and biochemicals.[24−28] In our previous work,[8] we extensively engineered 6PGDH from *T. maritima* to boost its activity on NMN$^+$, and the NMN$^+$-dependent specific activity of the optimal mutant was ∼30 times higher than that of the WT enzyme. While, the engineering of G6PDH from *T. maritima* had its limitations, as the specific activity on NMN$^+$ was only improved by 1.8-fold compared with the WT enzyme. However, the G6PDH-dependent regeneration of the reduced coenzyme is a promising alternative for glucose detection and G6P biosensing.[29−31] Therefore, enhancing the catalytic efficiency of G6PDH on BNCs could open an avenue for producing medium to low-cost products and determining glucose.

Herein, we engineered a high-activity NAD(P)$^+$-dependent G6PDH (GenBank accession number: AHJ70511) from *Zymomonas mobilis* via a semi-rational design, increasing its catalytic efficiency on NMN$^+$ by ∼112 times compared with the WT enzyme. Then, we determined the crystal structures and molecular dynamics (MD) simulations were performed to elucidate the mechanism of the enhanced catalytic efficiency of the G6PDH mutants on the regeneration of reduced nicotinamide mononucleotide (NMNH) from NMN$^+$. Furthermore, the optimal mutant of G6PDH was applied to a glucose biosensor constructed via the coimmobilization of glucokinase (EC 2.7.1.1, GK)[32] on a single-walled carbon nanotube (SWCNT)-modified glassy carbon electrode (GCE). This example, involving the coenzyme engineering of oxidoreductase, provided a lucrative possibility for regenerating and applying reduced synthetic BNCs. Not only does this study delineate the mechanism underpinning the enhanced catalytic efficiency of the G6PDH mutants on NMN$^+$ but it may also provide an alternative perspective for engineering dehydrogenases having a similar structure with G6PDH on NMN$^+$ and other BNCs.

MATERIALS AND METHODS

Chemicals and Strains. All chemicals were reagent grade and purchased from Sigma-Aldrich (St. Louis, MO) or Sinopharm (Shanghai, China) unless otherwise noted. The water-soluble redox dye WST-1 (2-(4-iodophenyl)-3-(4-nitrophenyl)-5-(2,4-disulfophenyl)-2H-tetrazolium) was obtained from Dojindo Laboratories (Kumamoto, Japan). *Escherichia coli* DH5α was used for plasmid construction, and BL21 (DE3)-containing protein expression plasmid was used to overexpress recombinant proteins, wherein cells were cultured in Luria−Bertani (LB) media supplemented with 100 μg/mL ampicillin or 50 μg/mL kanamycin.

Plasmid Construction and Mutagenesis. A plasmid pET28a-P*tac*-*g6pdh* that was under the control of a dual-promoter P*T7*-P*tac* encoding the *Z. mobilis* G6PDH thermostable mutant 4-1 was obtained as described elsewhere.[33] The plasmids pET20b-*di* and pET20b-*gk* containing diaphorase gene from *Geobacillus stearothermophilus* (DI, EC 1.6.99.3, GenBank accession number: JQ040550)[34] and glucokinase gene from *T. maritima* (GK, EC 2.7.1.1, GenBank accession number: AAD36537), respectively, were prepared as described elsewhere.[32] Herein, a site-directed saturation mutation library of G6PDH was constructed via a pair of primers containing the NNK codon at specified sites using a Phusion site-directed mutagenesis kit (Catalog Number F541; Thermo Scientific). Iterative saturation mutation (ISM) libraries were generated on each of the selected residues and then separately transformed into *E. coli* cells for subsequent plate-dependent high-throughput screening.

High-Throughput Screening of G6PDH Variants. As shown in Figure S1A, a plate-dependent high-throughput screening method was performed to identify positive NMN$^+$-active G6PDH mutants.[8] Following incubation and growth at 37 °C, the colonies on the Petri dish were heated at 70 °C for 1 h to improve cell membrane permeability, deactivate *E. coli* dehydrogenases, degrade endogenous reducing coenzymes, and provide heat-resistant selection pressure to G6PDH mutants. Subsequently, the colonies were transferred onto a filter paper and washed twice with phosphate-buffered saline (PBS) to reduce background noise. Finally, the washed, colony-stained filter paper was color developed using a second 0.5% agarose-containing solution for 1 h at room temperature of about 25 °C, which comprised 150 μM WST-1, 0.13 μM DI, 2.0 mM G6P, 1.0 mM NMN$^+$, 50 mM Tris-HCl (pH 7.5), and 50 μg/mL chloramphenicol. With the assistance of DI, the NMNH produced by G6PDH reduced WST-1 to reduced WST-1 formazan, developing a yellow color in the process (Figure S1B). For screening mutants in the random mutant library, the NMN$^+$ concentration in the agarose-containing solution was reduced to 0.5 mM, and the duration of color development was shortened to 30 min for higher screening stringency. The mutants exhibiting strong yellow color on the filter paper were selected and used for plasmid extraction.

Activity and Kinetic Assay of Recombinant Enzymes. His-tagged G6PDHs and GK were purified using the Ni-NTA column. Protein homogeneity was assessed using 12% sodium dodecyl sulfate−polyacrylamide gel electrophoresis, and protein concentrations were determined using the Bradford method with bovine serum albumin as the standard. The specific activity of G6PDHs was determined at 37 °C in 100 mM HEPES buffer (pH 7.5) containing 2.0 mM G6P, 1.0 mM of different types of coenzymes (NAD$^+$, NADP$^+$, or NMN$^+$), 5.0 mM $MgCl_2$, and 0.5 mM $MnCl_2$. The concentration of generated NADPH or NMNH was determined at 340 nm with a millimolar extinction coefficient of 6.22 mM^{-1} cm^{-1}.[8] One unit of G6PDH activity was defined as the amount of enzyme

https://doi.org/10.1021/acscatal.2c04707
ACS Catal. 2023, 13, 1983−1998

that released 1 μmol NADPH or NMNH/min. The steady-state kinetics of G6PDHs in the abovementioned reaction solution were measured using 2.0 mM G6P and variable concentrations of NAD^+, $NADP^+$, or NMN^+ at 37 °C.[33] The Michaelis−Menten kinetic parameters K_m and turnover number k_{cat} of G6PDHs were calculated based on the Michaelis−Menten equation via nonlinear regression using GraphPad Prism 5.01 software (San Diego, CA). The full steady-state kinetics of G6PDHs in the abovementioned reaction solution were measured using variable concentrations of coenzymes (10−200 μM $NADP^+$, 50−1000 μM NAD^+, or 5−100 mM NMN^+) and 50−1000 μM G6P at 37 °C. For full steady-state kinetic parameter analysis, the results were fitted to the ordered bi−bi rate equation, as described by Kanji.[35] The kinetic constants were estimated using nonlinear least square regression (SigmaPlot 12.5, San Jose, CA). The activity of GK was measured at 37 °C in 100 mM HEPES buffer (pH 7.5) containing 10 mM glucose, 1.0 mM ATP, and 5.0 mM $MgCl_2$. The reaction was stopped by $HClO_4$, followed by the neutralization with KOH.[36] The concentration of G6P was measured in a solution containing 100 mM HEPES buffer (pH 7.5), 1.0 U/mL *Z. mobilis* G6PDH, 1.5 mM NAD^+, and 5.0 mM $MgCl_2$ by determining the absorbance increase at 340 nm. One unit of GK activity was defined as the amount of enzyme that released 1.0 μmol G6P/min. Unless otherwise stated, each measurement was conducted in triplicate.

Crystallization and Structure Determination. The WT ZmG6PDH in the buffer (25 mM Tris-Cl and 150 mM NaCl, pH 7.5) was crystallized via the sitting-drop vapor diffusion method using a polyethylene glycol (PEG)/Ion 2 Screen Kit (Hampton Research, Laguna Niguel, CA). The initial reservoir solution (No. 5) contained 0.1 M sodium malonate (pH 6.0) and 12% w/v PEG 3350. The optimized crystals were obtained from the reservoir composition of 0.1 M sodium malonate (pH 6.0) and 10% w/v PEG 3350. The mutant ZmG6PDH R4 in buffer (25 mM Tris-Cl and 150 mM NaCl, pH 7.5) was crystallized via the sitting-drop vapor diffusion method using a MembFac Kit (Hampton Research, Laguna Niguel, CA). The initial reservoir solution (No. 44) contained 0.1 M diammonium hydrogen phosphate, 0.1 M Tris hydrochloride (pH 8.5), and 12% w/v PEG 6000. The optimized crystals were obtained from the reservoir composition of 0.2 M diammonium hydrogen phosphate, 0.1 M Tris hydrochloride (pH 8.5), and 14% w/v PEG 6000. All crystals were stored at 16 °C for 12 days to reach a suitable size for X-ray diffraction. The complex crystals were obtained by soaking the WT ZmG6PDH or ZmG6PDH R4 crystals in their corresponding reservoir solution containing 1.0, 5.0, and 10 mM coenzyme ($NADP^+$ or NMN^+) for 24 h. Finally, R4:NMN^+ was crystallized by soaking the R4 crystals in stock liquid containing 1.0 mM NMN^+.

Data were collected at beamline BL18U1 in Shanghai Synchrotron Radiation Facility (Shanghai, China) and processed using the HKL-3000 package,[37] the XDS and CCP4 suite.[38,39] The crystal structure of WT in the apo form (apo-WT) was resolved via the molecular replacement method using glucose-6-phosphate dehydrogenase from *Homo sapiens* (Protein Data Bank [PDB code: 6E08]) as the protein model. Similarly, the crystal structure of R4:NMN^+ was resolved via the molecular replacement method using apo-WT as the protein model. Subsequent structural refinements were performed using the programs Coot[40] and Phenix.[41] The data collection and refinement statistics of the G6PDH crystal structures are listed in Table S1 and have been deposited in the PDB under the accession code 7XHP for apo-WT and 7XHL for R4:NMN^+. All of the structural figures were prepared using PyMOL (http://pymol.sourceforge.net/).

System Preparation and Setup for Molecular Dynamics Simulation. To obtain insights regarding the influence of mutations on the enhanced coenzyme catalytic efficiency, MD simulations were performed for the enzyme/substrate (G6P)/coenzyme ternary complexes of WT and R4-type G6PDH and coenzyme ($NADP^+$ and NMN^+). In total, four ternary complexes named WT:$NADP^+$:G6P, WT:NMN^+:G6P, R4:$NADP^+$:G6P, and R4:NMN^+:G6P were obtained. The apo-WT enzyme crystal structure was used to construct the WT:$NADP^+$:G6P model. The $NADP^+$ coenzyme and the G6P substrate were placed in the active site of the apo-WT enzyme by overlapping the protein backbone with the reported G6PDH:G6P:NADPH ternary complex from *Trypanosoma cruzi* (PDB ID is 5AQ1).[42] The last snapshot from the MD equilibration step of the WT:$NADP^+$:G6P model was considered as the initial structure for establishing the WT:NMN^+:G6P model. In this model, the NMN^+ molecule was placed in the active site by fitting the nicotinamide ring of NMN^+ with $NADP^+$ in the short MD-equilibrated structure. For the R4:NMN^+:G6P model, the obtained crystal structure of R4:NMN^+ was considered as the starting point, and the substrate was manually added into the binding site using the G6PDH:G6P:NADPH ternary complex (PDB ID is 5AQ1, from *T. cruzi*) as the reference.[42] The R4:$NADP^+$:G6P model was constructed by overlapping the nicotinamide moiety of the $NADP^+$ molecule with NMN^+ in the R4:NMN^+:G6P model, followed by modifying the configuration of the remaining part of the $NADP^+$ molecule to fit the binding site of the model. During the modification, the $NADP^+$ binding site of the reported G6PDH:G6P:NADPH ternary complex (PDB ID is 5AQ1) was used as the reference.

The Amber ff14SB force field[43,44] was employed to evaluate the protein. The parameters for the substrate and cofactors were generated via the antechamber module using the general AMBER force field (gaff2),[45] and the partial charges were obtained via the restrained electrostatic potential method at the HF/6-31G* level.[46,47] All of the missing hydrogen atoms were added using the leap module of Amber 18.[48] Each system was subsequently immersed in a truncated octahedral TIP3P[49] water box with a spacing distance of 10 Å around the protein boundary. Finally, the obtained systems were neutralized by adding Na^+ to the protein surface.

Molecular Dynamics Simulations. The resulting systems were then subjected to two steps of energy minimization. First, the protein−substrate complex was restrained using a force constant of 5.0 kcal/(mol·Å^2), while the solvent molecules and ions in the system were fully optimized (5000 steps for the steepest descent and conjugate gradient each). Subsequently, the restraint was only kept for the protein backbone, whereas the remaining system was optimized. The systems were then heated from 10 to 300 K under NVT ensemble in 50 ps with a harmonic potential of 5 kcal/(mol·Å^2) on the solute, followed by 500 ps density equilibration under the NPT ensemble at a constant temperature of 300 K and a target pressure of 1.0 bar. Following this, 20 ns productive MD simulations were performed for each system under the NPT ensemble, and the initial 1.0 ns trajectory was excluded from the analysis. All of the covalent bonds involving hydrogen were constrained using the SHAKE algorithm.[50] The particle mesh Ewald

https://doi.org/10.1021/acscatal.2c04707
ACS Catal. 2023, 13, 1983−1998

Table 1. Apparent Kinetic Parameters of WT ZmG6PDH and its Mutants toward NAD^+, $NADP^+$, and NMN^+[a]

	NAD^+				$NADP^+$			
enzyme	sp. act. (U/mg)	K_m (μM)	k_{cat} (s^{-1})	k_{cat}/K_m (mM^{-1} s^{-1})	sp. act. (U/mg)	K_m (μM)	k_{cat} (s^{-1})	k_{cat}/K_m (mM^{-1} s^{-1})
WT	$(1.3 \pm 0.076) \times 10^2$	$(4.0 \pm 0.063) \times 10^2$	$(1.7 \pm 0.012) \times 10^2$	$(4.2 \pm 0.074) \times 10^2$	$(1.5 \pm 0.054) \times 10^2$	$(7.7 \pm 0.54) \times 10^1$	$(1.9 \pm 0.058) \times 10^2$	$(2.4 \pm 0.12) \times 10^3$
R1	$(9.7 \pm 0.14) \times 10^1$	$(4.2 \pm 0.24) \times 10^2$	$(7.4 \pm 0.20) \times 10^1$	$(1.7 \pm 0.13) \times 10^2$	$(1.1 \pm 0.027) \times 10^2$	$(6.5 \pm 0.32) \times 10^1$	$(8.4 \pm 0.15) \times 10^1$	$(1.3 \pm 0.031) \times 10^3$
R2	$(2.9 \pm 0.12) \times 10^1$	$(4.1 \pm 0.35) \times 10^2$	$(1.3 \pm 0.051) \times 10^1$	$(3.3 \pm 0.072) \times 10^1$	$(2.2 \pm 0.060) \times 10^1$	$(7.0 \pm 0.37) \times 10^1$	$(1.6 \pm 0.045) \times 10^1$	$(2.3 \pm 0.084) \times 10^2$
R3	7.3 ± 0.33	$(3.0 \pm 0.30) \times 10^2$	4.6 ± 0.18	$(1.5 \pm 0.14) \times 10^1$	$(1.0 \pm 0.054) \times 10^1$	$(4.6 \pm 0.33) \times 10^1$	8.3 ± 0.22	$(1.8 \pm 0.062) \times 10^2$
R4	6.2 ± 0.26	$(3.7 \pm 0.35) \times 10^2$	3.7 ± 0.15	$(1.0 \pm 0.073) \times 10^1$	6.6 ± 0.52	$(6.0 \pm 0.28) \times 10^1$	6.3 ± 0.14	$(1.1 \pm 0.012) \times 10^2$

	NMN^+				fold	
enzyme	sp. act. (mU/mg)	K_m (mM)	k_{cat} (s^{-1})	k_{cat}/K_m (mM^{-1} s^{-1})	F_{NAD^+}	F_{NADP^+}
WT	4.3 ± 0.072	$(3.6 \pm 0.37) \times 10^1$	$(1.5 \pm 0.072) \times 10^{-1}$	$(4.2 \pm 0.82) \times 10^{-3}$	1.0	1.0
R1	$(5.2 \pm 0.33) \times 10^1$	$(4.3 \pm 0.51) \times 10^1$	1.9 ± 0.14	$(4.4 \pm 0.32) \times 10^{-2}$	2.5×10^1	2.0×10^1
R2	$(1.8 \pm 0.17) \times 10^2$	$(2.2 \pm 0.33) \times 10^1$	4.0 ± 0.23	$(1.9 \pm 0.044) \times 10^{-1}$	5.9×10^2	4.9×10^2
R3	$(2.4 \pm 0.14) \times 10^2$	$(2.2 \pm 0.32) \times 10^1$	6.5 ± 0.55	$(2.9 \pm 0.073) \times 10^{-1}$	1.9×10^3	9.3×10^2
R4	$(3.4 \pm 0.13) \times 10^2$	$(1.8 \pm 0.10) \times 10^1$	8.6 ± 0.23	$(4.7 \pm 0.24) \times 10^{-1}$	4.7×10^3	2.6×10^3

[a]Steady-state kinetics of ZmG6PDHs were measured in 100 mM HEPES buffer (pH 7.5) containing 2 mM G6P, 5 mM $MgCl_2$, and 0.5 mM $MnCl_2$ with a variable concentration of NAD^+ (100−1000 μM), $NADP^+$ (6.25−300 μM), or NMN^+ (5−100 mM) at 37 °C. The coenzyme specificity value of an enzyme is the ratio of the catalytic efficiency value of this enzyme on NMN^+ with those on NAD^+ or $NADP^+$, respectively, which were $[k_{cat}/K_m]_{NMN}{}^+/[k_{cat}/K_m]_{NAD}{}^+$ and $[k_{cat}/K_m]_{NMN}{}^+/[k_{cat}/K_m]_{NADP}{}^+$. Fold change improvement is defined as the ratio of the coenzyme specificity value between an enzyme and the WT enzyme. $F_{NAD}{}^+$ is the ratio of the $[k_{cat}/K_m]_{NMN}{}^+/[k_{cat}/K_m]_{NAD}{}^+$ value between an enzyme and the WT enzyme, and $F_{NADP}{}^+$ is the ratio of the $[k_{cat}/K_m]_{NMN}{}^+/[k_{cat}/K_m]_{NADP}{}^+$ value between an enzyme and the wild-type enzyme. WT, wild-type ZmG6PDH; R1, S115A; R2, S115A/P118S/Y417H; R3, S115A/P118S/Y417H/M421L; R4, S25A/S115A/P118S/Y417H/M421L. Values shown are means of triplicate determinations.

https://doi.org/10.1021/acscatal.2c04707
ACS Catal. 2023, 13, 1983−1998

algorithm[51] was used to calculate long-range electrostatic interactions. We used a time step of 2.0 fs for the entire simulation. The periodic boundary conditions were employed throughout the simulations, and the cutoff region for space Coulomb and van der Waals (vdW) forces was 8.0 Å. To obtain the most populated structures, the MD trajectories were clustered using the CPPTRAJ module of Amber 18.[52] The binding free energies were evaluated via the Molecular Mechanical Poisson−Boltzmann Surface Area (MM-PBSA) calculations based on the trajectories obtained from the last 5.0 ns of the MD simulations.

Glucose Biosensor. Single-walled carbon nanotubes (SWCNTs, purchased from Carbon Solutions, Inc [Riverside, CA]) were activated by glutaraldehyde, conjugating nitrilotriacetate groups, and chelating Ni^{2+} to form functionalized SWCNTs.[53] The overexpressed His-tagged enzymes attached to the Ni^{2+}-modified SWCNTs. Herein, GK and G6PDH mutant R4 were mixed in a specific activity ratio of 1:1 in PBS to prepare enzyme solutions with total protein concentrations of 2.0, 4.0, 6.0, and 8.0 g/L. Then, 40 μL of enzyme solution was poured into 40 μL of 15 mg/mL SWCNT dispersion and crosslinked at room temperature for 1.0 h under oscillation. Next, the crosslinked product was washed thrice with PBS to remove unbound GK and R4, thereby yielding a GK-R4/SWCNT complex. The concentrations of the unbound protein were determined using the Bradford method, and the amount of immobilized enzymes was also calculated. A transmission electron microscope (HT7700, Hitachi, Japan) was used to assess the GK-R4/SWCNT composite. The fluorescein isothiocyanate (FITC)-labeled GK-R4/SWCNT complex was examined using a laser scanning confocal microscope (TCS SP5 II, Leica, Germany) with a peak excitation wavelength of 570 nm.[54]

While preparing GK-R4/SWCNTs/GCE, the redispersed GK-R4/SWCNT complex was dripped on the polished GCE (3 mm in diameter) surface and dried at room temperature for 2.0 h. The electrochemical tests were conducted using the differential pulse voltammetry (DPV) method on a CHI660E electrochemical workstation (Shanghai Chenhua Instrument, China). All measurements of DPV scanning were performed at 37 °C in a 5-mL anolyte with 100 mM HEPES buffer (pH 7.5) containing 5.0 mM $MgCl_2$, 0.5 mM $MnCl_2$, 100 mM NaCl, 2.0 mM NMN^+, and 5.0 mM ATP using a three-electrode system with the GK-R4/SWCNTs/GCE as the working electrode, Ag/AgCl as the reference electrode, and Pt wire as the counter electrode. When determining the glucose concentration in real samples using this NMN^+-based biosensor, the samples were first diluted to ensure that the glucose concentration fell within the linear range for detecting this biosensor. The tests with 0 mM coenzyme, 2.0 mM NAD^+, and 2.0 mM $NADP^+$ were performed as control reactions. Moreover, the concentration of glucose in the real samples was measured to compare via a high-performance liquid chromatography (HPLC) apparatus equipped with a Bio-Rad HPX-87H column and a refractive index detector using 5.0 mM H_2SO_4 as a mobile phase.

RESULTS

Enzymatic Properties of ZmG6PDH and Its Crystal Structure. To efficiently regenerate NMNH, we engineered G6PDH to increase its coenzyme catalytic efficiency on NMN^+. Comprehensively considering thermostability, protein expression levels, and initial NMN^+ activity, a G6PDH from *Z. mobilis* (ZmG6PDH) was selected as the WT enzyme in this study. The ZmG6PDH enzyme showed >50% soluble expression level in BL21(DE3) (Figure S2). The specific activity values of WT ZmG6PDH on NAD^+, $NADP^+$, and NMN^+ were ~1.3×10^2 U/mg, 1.5×10^2 U/mg, and 4.3 mU/mg at 37 °C, respectively. The kinetic parameters of ZmG6PDH were investigated using NAD^+, $NADP^+$, and NMN^+ as the coenzymes (Table 1). The WT ZmG6PDH is highly specific for regenerating NADPH using G6P as the sacrificed substrate, with a K_m of ~7.7×10^1 μM, k_{cat} of ~1.9×10^2 s^{-1}, and catalytic efficiency (k_{cat}/K_m) of ~2.4×10^3 mM^{-1} s^{-1} on $NADP^+$, whereas this enzyme exhibited a low NMNH regeneration activity with a catalytic efficiency of ~4.2×10^{-3} mM^{-1} s^{-1}. Compared with $NADP^+$, the WT ZmG6PDH showed a 5.2-fold higher K_m and similar k_{cat} when using NAD^+ as the coenzyme, providing k_{cat}/K_m of ~4.2×10^2 mM^{-1} s^{-1} on NAD^+.

To increase the activity of ZmG6PDH for NMNH regeneration, we used an enzyme engineering strategy based on structural information. The crystal structure of WT ZmG6PDH in the apo form (apo-WT) was resolved successfully at a resolution of 2.78 Å in the *P*1211 space group. There were eight molecules in an asymmetrical unit, which was formed by stacking four homodimer functional units (Figure 1B). The eight monomers in the asymmetrical unit demonstrated high similarity with the measured root-mean-square deviation (RMSD) values of ~0.2 Å. The overall structure of the G6PDH monomer comprised Rossmann-like and β+α domains (Figure 1C). The sequence alignment of ZmG6PDH and other homologous sequences indicated that D173 and H236 were the catalytic residues (Figure S3). Our attempts to determine the crystal structure of WT ZmG6PDH in complex with $NADP^+$ were unsuccessful; therefore, the molecule F in the crystallized apo-WT was used for the following investigation to bind with $NADP^+$ *in silico*.

Evolution of NMN^+-Based G6PDH Mutants. Based on the crystal structure of molecule F of apo-WT, the $NADP^+$-docked WT ZmG6PDH model (WT:$NADP^+$) (energy minimized using Chem3D 15.1) was generated via AutoDock version 4.2.6 (https://autodock.scripps.edu/) (Figure 1D). In this docking model, $NADP^+$ was bound into the enzyme pocket, exhibiting a network of hydrogen bonds and van der Waals interactions. Compared with NAD^+ and $NADP^+$, NMN^+ lacked the adenosine monophosphate moiety; thus, the interaction network between the NMN^+ part of $NADP^+$ and WT ZmG6PDH was addressed first. Potential hydrogen-bond interactions were observed between the O atom of bisphosphate of $NADP^+$ and the main-chain N atom of L17, as well as the nicotinamide amide and side-chain O atom of D16 (Figure 1D). These two residues (D16 and L17) of ZmG6PDH were the nucleotide-binding fingerprint in the βA-αa turn.[55] In addition, the main chain of residues T116 and K144 formed hydrogen bonds to the ribose O atoms of $NADP^+$. Apart from these four residues, the other 11 resides (G15, S18, R20, M21, S115, S117, P118, F121, E143, P145, and Y417) that were located adjacent (<5 Å) to NMN^+ in $NADP^+$ in the coenzyme-binding sites of ZmG6PDH were also selected as candidates for the following mutations (Figure 1D).

First, alanine-scanning mutagenesis was performed on these 15 residues. The optimal mutant S115A, termed R1, exhibited a 12-fold increase in specific activity for NMN^+ and ~30% decrease for $NADP^+$ (Table 1). Subsequently, the ISM libraries were constructed for the other 14 residues based on the mutant R1. Using a plate-dependent high-throughput screen-

https://doi.org/10.1021/acscatal.2c04707
ACS Catal. 2023, 13, 1983−1998

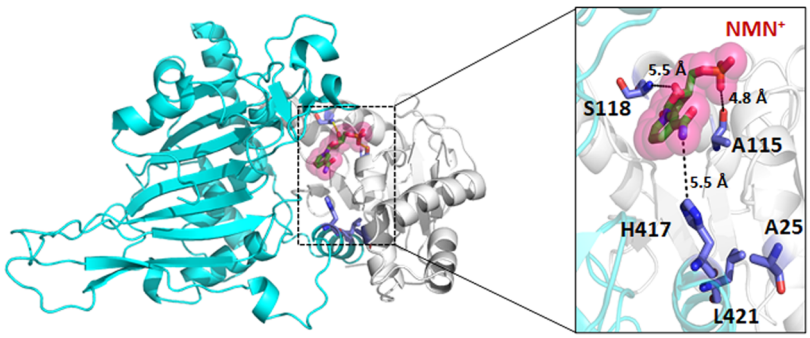

Figure 2. Crystal structure of the monomer complex of the ZmG6PDH R4 mutant and NMN^+ (R4:NMN^+). Five positive residues (A25, A115, S118, H417, and L421) were highlighted. The coenzyme-binding and catalytic domains are represented in gray and cyan, respectively. Black dashed lines indicate the distance of residues to NMN^+.

ing method,[8] the colonies with the greatest color intensity were excavated from each site-directed saturation mutagenesis library following color development owing to the presence of WST-1 in the second solution (Figure S4A). Ultimately, two mutants (S115A/P118S and S115A/Y471H) that exhibited beneficial effects on NMN^+ activity were obtained in the second-round mutation experiment (Table S2). The combination of these mutants yielded the S115A/P118S/Y471H mutant (R2), indicating a potential synergistic effect between these mutation sites on the enhanced catalytic activity of ZmG6PDH on NMN^+ (Table 1). No positive site was observed in the ISM experiment in the remaining 12 residues. To break this barrier, 54 residues in ZmG6PDH, which were located within 5.0−12 Å of the NMN^+ moiety in $NADP^+$, were selected to undergo ISM based on R2 (Figure S5). Following two rounds of sequential high-throughput screening, positive mutants S115A/P118S/Y471H/M421L (R3) and S25A/S115A/P118S/Y471H/M421L (R4) were obtained. Compared with the WT ZmG6PDH, the mutant R4 exhibited a sharp difference in the intensity of coloration on the plate (Figure S4B). The measured specific activity of the purified mutant R4 on NMN^+ was ∼78 times higher than that of WT ZmG6PDH, while the specific activity values of NAD^+ and $NADP^+$ were only ∼4.9 and 4.3% of the WT ZmG6PDH, respectively (Table 1).

Kinetic Parameters of ZmG6PDH Mutants. The kinetic parameters of all of the mutants and WT ZmG6PDH for NAD^+, $NADP^+$, and NMN^+ were determined. Overall, as the number of mutant residues increased, k_{cat} of NAD^+ and $NADP^+$ and K_m of NMN^+ decreased and k_{cat} of NMN^+ increased (Table 1). This phenomenon gradually increased k_{cat}/K_m of NMN^+ and decreased k_{cat}/K_m of NAD^+ and $NADP^+$ of the mutants. In the first round of mutation, k_{cat}/K_m of R1 on NAD^+ and $NADP^+$ were reduced to ∼41 and 53% of the WT enzyme, respectively, while k_{cat}/K_m of NMN^+ was ∼10-fold higher than that of the WT enzyme. In the second-round mutation, k_{cat}/K_m of S115A/P118S on $NADP^+$ was lower than that of S115A/Y417H, and k_{cat}/K_m of both the mutants on NMN^+ were equivalent (Table S2). Compared with R1, k_{cat}/K_m of R2 on NAD^+ and $NADP^+$ were reduced to ∼19% and 18%, respectively, and k_{cat}/K_m of NMN^+ was increased by ∼4.2 times. Furthermore, k_{cat}/K_m of mutants S115A/P118S/Y471H/M421L (R3) and S25A/S115A/P118S/Y471H/M421L (R4) exhibited a continuous decreased and increased catalytic efficiency on $NAD(P)^+$ and NMN^+, respectively. Significantly, all of the mutations exhibited a continuous decrease of K_m on NMN^+. The K_m of R4 was ∼51% of that of the WT enzyme. Conversely, k_{cat} of R4 on NAD^+ and $NADP^+$ were ∼2.2% and 3.4% of the WT enzyme, respectively, and k_{cat} of R4 on NMN^+ was ∼57 times that of the WT enzyme, yielding a ∼112-fold enhancement in catalytic efficiency (k_{cat}/K_m) on NMN^+. Collectively, the two coenzyme specificity values ($[k_{cat}/K_m]_{NMN^+}/[k_{cat}/K_m]_{NAD^+}$ and $[k_{cat}/K_m]_{NMN^+}/[k_{cat}/K_m]_{NADP^+}$) of the R4 mutant were ∼4.7×10^3 and 2.6×10^3-fold of the WT enzyme, respectively (Table 1). Additionally, the enhanced catalytic efficiency of ZmG6PDH for NMN^+ did not sacrifice its thermostability (Figure S6).

Structural Insights into NMN^+-Active Mutant R4. To gain insights into the enhanced catalytic efficiency on NMN^+ of the R4 mutant, we obtained the cocrystal structure of R4 with NMN^+ (R4:NMN^+) in a space group *P*1211 at a resolution of 3.25 Å. In the R4:NMN^+ crystal structure, the R4 mutant formed a homooctamer that was similar to the structures of WT ZmG6PDH, and the monomers A, B, E, and G were R4:NMN^+ complexes (Figure S7). Monomer G was selected as the enzyme−coenzyme complex for the following studies owing to its complete protein chain structure and well-matched coenzyme electron density map (PDB code 7XHL for R4:NMN^+).

The cocrystal structure R4:NMN^+ demonstrated that NMN^+ binds at the coenzyme-binding Rossmann-like domain, wherein the main chain of D16 and L17 formed hydrogen bonds with the O atom of the phosphate in NMN^+, and the main chain of T116 and the side chain of E143 formed hydrogen bonds with the O atoms of ribose in NMN^+ (Figure S8). Compared with the hydrogen-bonding network in the $NADP^+$-docked WT model (Figure 1D), the hydrogen bonds between the residues D16, L17, T116, and the coenzyme were retained. The only difference among the binding pockets of these models was the hydrogen bond between K144 and $NADP^+$ in the docking structure of WT:$NADP^+$ and the hydrogen bond between E143 and NMN^+ in the cocrystal structure of WT:NMN^+. In addition, three (S115A, P118S, and Y417H) of the five positive mutation residues were adjacent to the active pocket in a region within 5.5 Å of NMN^+ (Figure 2). As all our attempts to obtain the crystal structure of the R4:$NADP^+$ complex were unsuccessful, the $NADP^+$-docked ZmG6PDH R4 model (R4:$NADP^+$) was obtained using AutoDock version 4.2.6. Subsequently, superimposing the obtained structure of R4:$NADP^+$ with R4:NMN^+ revealed that the binding of the nicotinamide section of NMN^+ in R4:NMN^+ was much closer to the residue H417 than that of $NADP^+$ (Figure S9A). The mutation site Y417H occupied smaller side-chain groups that provided more space for the

https://doi.org/10.1021/acscatal.2c04707
ACS Catal. 2023, 13, 1983−1998

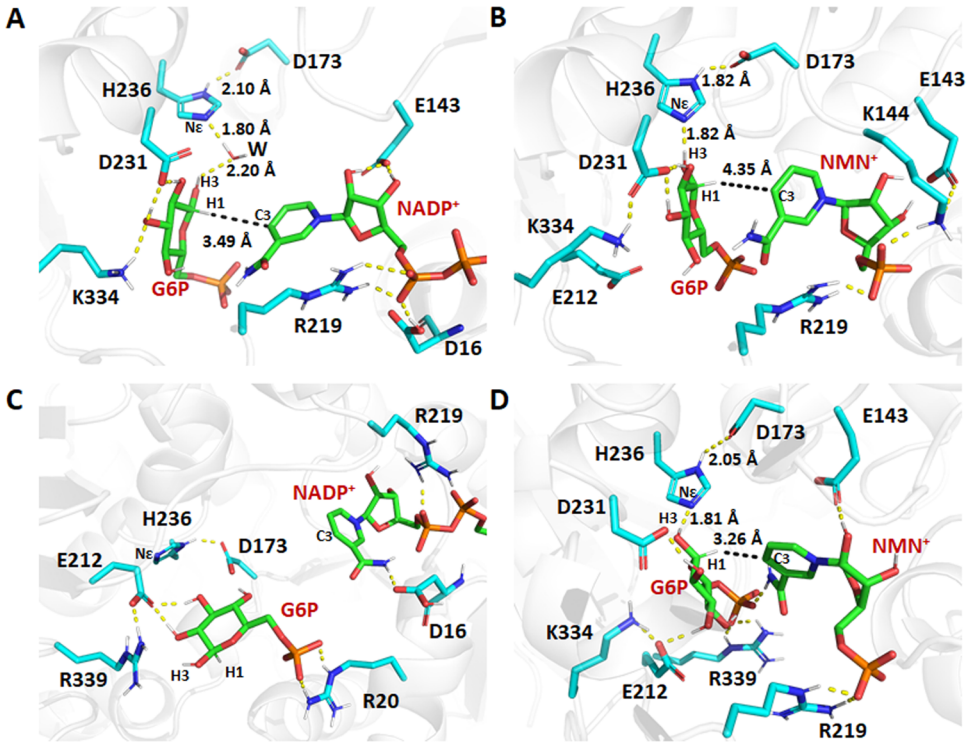

Figure 3. Most representative structures from the largest cluster of the MD trajectory of the (A) WT:NADP$^+$:G6P, (B) WT:NMN$^+$:G6P, (C) R4:NADP$^+$:G6P, and (D) R4:NMN$^+$:G6P models. The hydrogen bonds and the lengths of the hydride transfer distances are shown in yellow and black dotted lines, respectively.

coenzyme and favored the entry of NMN$^+$ into the active center for the catalytic reaction. After comparing the obtained crystal structures of apo-WT and R4:NMN$^+$, the loop and α-helix domain near the cofactor binding site of R4:NMN$^+$ exhibited a significant shift toward NMN$^+$. As the S115A and P118S mutations were located in the loop area adjacent to NMN$^+$, these mutations were likely to facilitate this transition to NMN$^+$ (Figure S9B), thereby potentially influencing both the binding affinities of NADP$^+$ and NMN$^+$ toward the R4 mutant. The presence of a proline residue usually engenders structural stability to the corresponding domain.[56,57] Thus, the P118S mutation may enhance the flexibility of the corresponding domain and facilitate the shift of the loop region toward the NMN$^+$ binding site (Figure S9B), thereby increasing the binding affinity of the R4 mutant toward the NMN$^+$ molecule. According to the induced fit theory, enzymes usually undergo conformational shifts once the substrate and cofactor are bound. As has been reported in the literature, compared with the apo-enzyme, a G6PDH from *Leuconostoc mesenteroides* (LmG6PDH) exhibited a relatively closed structural conformation after binding with the coenzyme.[55] This phenomenon is consistent with our observations in ZmG6PDH.

Unfortunately, owing to the distance of the mutations (>10 Å to NMN$^+$), the S25A and M421L mutations did not directly affect coenzyme binding in the R4:NMN$^+$ structure. At the interface of the Rossmann-like domain (coenzyme-binding domain) and the β+α domain (substrate-binding domain) in ZmG6PDH, the helices αl and αm interacted across the domain boundary with several elements of the coenzyme-binding domain, such as αa, αa-βB turn, αf, and carboxyl termini of the sheet strands βD and βE. Remarkably, the residues 25 and 421 were located at the surface junction. Therefore, a reasonable hypothesis can be proposed that the mutants M421L and S25A contributed to the enhanced catalytic efficiency on NMN$^+$ by adjusting and stabilizing the interface interactions between the domains by introducing relative hydrophobic residues. As the crystal structure resolution of R4:NMN$^+$ is not sufficiently high and lacks the crystal structures of apo-R4 and WT:NMN$^+$, the above-mentioned speculation cannot be confirmed via effective comparative analysis. Therefore, MD simulations were applied to analyze the mechanism of enhanced catalytic efficiency of the ZmG6PDH mutant on NMN$^+$.

MD Simulation to Elucidate the Enhanced Catalytic Efficiency of R4 Mutant on NMN$^+$. As described in the Materials and Methods section, four ternary complexes of ZmG6PDH (WT and R4), substrate G6P, and coenzyme (NADP$^+$ and NMN$^+$) were established and termed as WT:NADP$^+$:G6P, WT:NMN$^+$:G6P, R4:NADP$^+$:G6P, and R4:NMN$^+$:G6P, respectively. The active site configuration of the last snapshot obtained from the density equilibration step of these four models (Figure S10) revealed that the hydrogen-bond network of these models exhibited a similar pattern. With these hydrogen-bond interactions, the binding pocket organized the substrate and coenzyme to a configuration that favored the hydride transfer from G6P to the C3 of nicotinamide in the coenzyme (Figure S10). Although the hydride transfer channel is reserved following the density equilibration of all of the four models, large differences were observed during the following 20 ns productive MD simulations.

The RMSDs of all of the simulations are shown in Figure S11. We performed clustering analysis to better analyze the conformations of the substrate and coenzyme in the different models. Based on the RMSDs of the residues within 6.0 Å of the substrate and coenzyme, the productive MD trajectories

https://doi.org/10.1021/acscatal.2c04707
ACS Catal. 2023, 13, 1983−1998

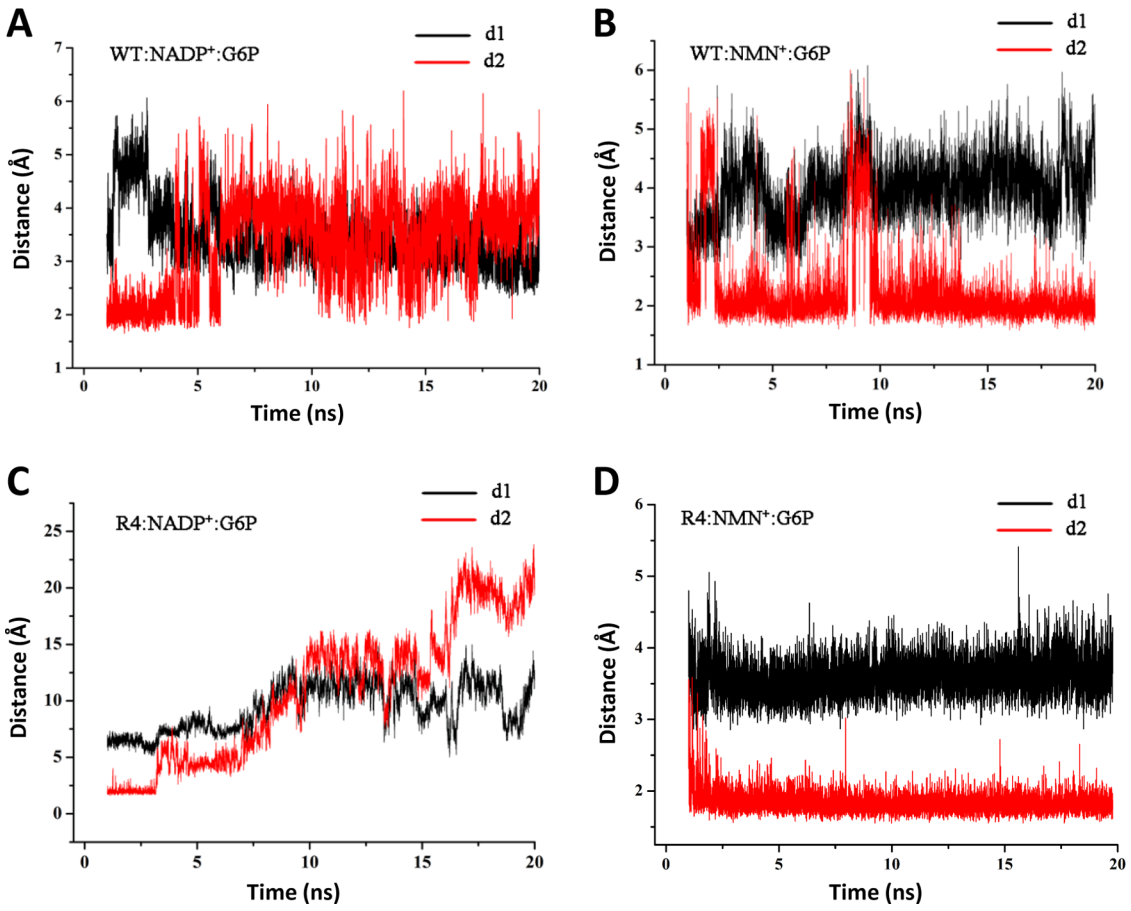

Figure 4. Changes in key distances during the MD simulations of the (A) WT:NADP$^+$:G6P, (B) WT:NMN$^+$:G6P, (C) R4:NADP$^+$:G6P, and (D) R4:NMN$^+$:G6P models. The hydride transfer distance $d_{H1\text{-}C3}$ from H1 of the substrate and C3 of the coenzyme was defined as d1. The proton transfer distance $d_{H3\text{-}N\varepsilon}$ between H3 of the substrate and Nε of H236 was defined as d2.

for each model were grouped into 10 clusters. Figure 3 presents the most representative snapshots from each model where considerable differences between these models were observed. To evaluate the feasibility of the hydride and proton transfer steps in the glucose oxidation reaction, two distances were considered the key criteria, namely, (1) the hydride transfer distance ($d_{H1\text{-}C3}$) defined by the length between H1 of the substrate and C3 of the coenzyme and (2) the proton transfer distance ($d_{H3\text{-}N\varepsilon}$) defined by the length between the H3 of the substrate and Nε of H236. As shown in Figure 3A,B, the proton transfer channels in both the WT:NADP$^+$:G6P and WT:NMN$^+$:G6P models were highly reserved, and the only difference was that the H3 of the substrate interacted with the Nε of H236 via a bridging water molecule in the WT:NADP$^+$:G6P model, whereas the H3 of the substrate directly formed a hydrogen bond with H236 in the WT:NMN$^+$:G6P model, indicating that the proton transfer processes in the two systems were plausible. For the $d_{H1\text{-}C3}$, the measured value in the WT:NADP$^+$:G6P model was ∼3.5 Å, which was extended to ∼4.4 Å in the WT:NMN$^+$:G6P model. Thus, the hydride transfer in the WT:NMN$^+$:G6P system was less favorable than that in WT:NADP$^+$:G6P. The representative structure of the R4:NADP$^+$:G6P model for the mutant R4 showed that the substrate G6P was bound at a position that was unfavorable for catalysis (Figure 3C). While for the R4:NMN$^+$:G6P model (Figure 3D), both the hydride and proton transfer pathways were well reserved ($d_{H1\text{-}C3}$ = 3.3 Å, $d_{H3\text{-}N\varepsilon}$ = 1.8 Å).

The evolution of the hydride and proton transfer distances during simulations is shown in Figure 4. In most trajectories of the WT:NADP$^+$:G6P model, the $d_{H1\text{-}C3}$ was at a distance of ∼3.5 Å (Figure 4A), whereas this distance was >4.0 Å in the WT:NMN$^+$:G6P model (Figure 4B). For the other distance $d_{H3\text{-}N\varepsilon}$, the value in the WT:NADP$^+$:G6P model vibrates ∼4.0 Å (Figure 4A). However, a stable water bridge was observed between the H3 of the substrate and the Nε of the H236 (as is also shown in the representative structure of the WT:NADP$^+$:G6P model in Figure 3A), facilitating proton transfer. For the R4:NADP$^+$:G6P model, as observed in Figure 4C, following 5 ns MD simulation, the hydride and proton transfer distances increased to an unfavorable value for the reaction to occur. Alongside the substrate G6P binding pattern in the representative snapshot of this model (Figure 3C), these results suggest that the R4:NADP$^+$:G6P model exhibits a lower G6P binding affinity than the WT:NADP$^+$:G6P model. Furthermore, the reduced binding affinity for G6P in the R4:NADP$^+$:G6P model has been validated by the full steady-state kinetic parameters, and the full steady-state Michaelis constant for G6P (K_B) in the R4:NADP$^+$:G6P model was ∼1.6 times higher than that of the WT:NADP$^+$:G6P model (Table S3). In the R4:NMN$^+$:G6P model, a stable hydrogen bond formed between H1 and H236, and in most of the trajectories, the distance of the potential hydride transfer reaction was <4.0 Å (Figure 4D). Therefore, our simulation results of the R4:NMN$^+$:G6P and WT:NMN$^+$:G6P models indicate that the R4 mutant exhibits higher catalytic activity on NMN$^+$ than

https://doi.org/10.1021/acscatal.2c04707
ACS Catal. 2023, 13, 1983−1998

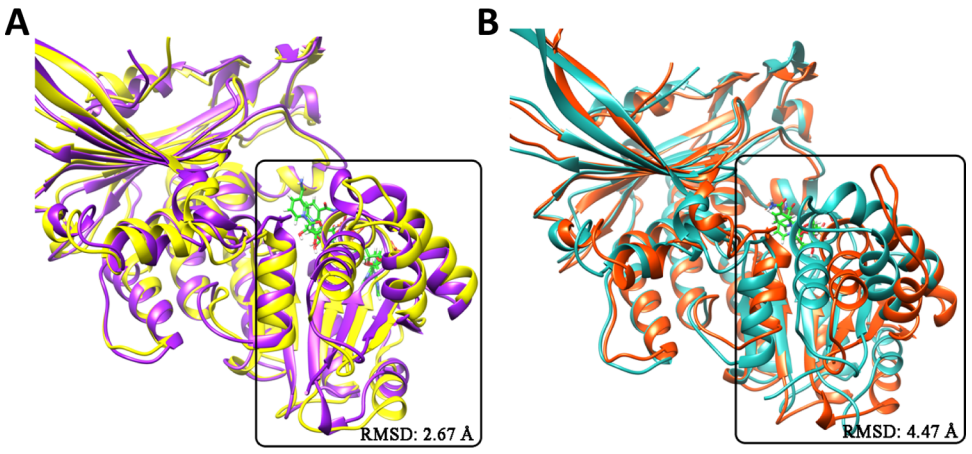

Figure 5. Superposition of the representative structures of (A) WT:NADP$^+$:G6P (yellow) and R4:NADP$^+$:G6P (purple) models and (B) WT:NMN$^+$:G6P (orange) and R4:NMN$^+$:G6P (blue) models. The black rectangle marks the region where the largest structural difference was observed.

WT. Following the analysis of the binding site of the cocrystal structure R4:NMN$^+$, the hydrogen bonds between D16, L17, T116, and E143 of the R4 and NMN$^+$ were also predicted by the MD simulations. Generally, the trajectory analysis results indicate that the WT enzyme exhibited higher activity on NADP$^+$ than on NMN$^+$, whereas the R4 mutant displayed much higher activity on NMN$^+$ than the WT enzyme. These results are consistent with experimental observations.

The binding free energies of the substrate in the four models were calculated using MM-PBSA. The calculated binding free energies for the WT:NADP$^+$:G6P, WT:NMN$^+$:G6P, R4:NADP$^+$:G6P, and R4:NMN$^+$:G6P models were −12.8, −2.6, −0.5, and −12.4 kcal/mol, respectively. Our calculation results indicate that the substrate-binding is more stable with NADP$^+$ as the coenzyme than NMN$^+$ in the WT models, whereas this trend was reversed in the R4 models, which exhibit lower substrate-binding free energy when bound with NMN$^+$ than when bound with NADP$^+$. The differences in the calculated substrate-binding free energies of these models might account for the observed enhanced catalytic efficiency of the R4 mutant on NMN$^+$. Thus, compared with the WT:NMN$^+$:G6P model, shorter hydride transfer distance and higher binding affinity of the substrate were observed for the R4:NMN$^+$:G6P model, indicating that the mutant R4 exhibited an increased catalytic efficiency on NMN$^+$.

To further explore how these mutations enhanced the catalytic efficiency of the enzymes on NMN$^+$, we analyzed the root-mean-square fluctuations of the enzymes during MD simulations (Figure S12). Compared with the WT enzyme, the mutant R4 exhibited a larger deviation in the helix region from D16 to E143. This region is the coenzyme-binding Rossmann-like domain that includes the sites of three mutations (S25, S115, and P118). By overlapping the most representative structures of the WT and R4 models, a clear drift of the helix region was observed for the WT:NMN$^+$:G6P and R4:NMN$^+$:G6P models, whereas no obvious helix region drift occurred in the WT:NADP$^+$:G6P and R4:NADP$^+$:G6P models (Figure 5). The calculated RMSD for the residues from D16 to E143 between the WT:NADP$^+$:G6P and R4:NADP$^+$:G6P models was ∼2.7 Å (Figure 5A), whereas the value calculated between the WT:NMN$^+$:G6P and R4:NMN$^+$:G6P models was ∼4.5 Å (Figure 5B). In the R4:NMN$^+$:G6P model, the helix region moves toward the active site pocket and thus was closer to the helical region where the Y417H and M421L mutations occurred, which favored the binding of a smaller coenzyme (NMN$^+$). As shown in Table S3, the full steady-state Michaelis constant of WT ZmG6PDH for NMN$^+$ (K_A) was ∼2.6 times higher than that of the R4 mutant, thereby demonstrating the enhanced NMN$^+$ binding ability of the R4 mutant. This result is consistent with that of MD simulations. In addition, the dissociation constant (k_{ia}) of WT ZmG6PDH on NADP$^+$ and NMN$^+$ were about 1.6- and 2.2-fold higher than that of the R4 mutant, respectively (Table S3), indicating an enhanced coenzyme-binding ability of R4 on both NADP$^+$ and NMN$^+$.

Furthermore, in the adenosine moiety binding site of the representative snapshot of the WT:NADP$^+$:G6P model (Figure S13), the oxygen in the side chain of S115 forms a hydrogen bond with the adenosine part of NADP$^+$, thereby facilitating the binding of NADP$^+$. When this residue is mutated to alanine, the hydrogen-bonding interaction breaks, and the hydrophobicity of the adenosine moiety binding area increases because of the higher hydrophobicity of alanine than serine,[58] and therefore, the NADP$^+$ binding affinity of the S115A mutant reduces. Owing to the presence of several hydrophobic residues (L10, L17, and L22) in the vicinity of the S115 mutant, the increased hydrophobicity of residue 115 might cause these other hydrophobic residues to be packed more closely, affording a smaller binding pocket, which may increase the enzyme binding affinity toward the smaller NMN$^+$. Moreover, the packing effect of A115 to the R4 mutant may be facilitated by the observed increased flexibility of the helix and loop regions (G109 to A131) in the MD simulations (Figure S12). Therefore, our simulation results suggest that the introduced mutations affect the motion of the helix regions near the active site, bringing them closer to the active site and favoring the binding of NMN$^+$.

Biomimetic NMN$^+$-Based Glucose Biosensor. Herein, the applicability of the NMN$^+$-active ZmG6PDH R4 was assessed in a two enzyme-facilitated glucose biosensing system as the thermostable R4 can function without cryopreservation. Glucokinase (EC 2.7.1.1, GK) catalyzes the conversion of glucose into G6P and ADP in the presence of ATP. Subsequently, ZmG6PDH R4 catalyzes the conversion of G6P to 6-phosphogluconolactone (6PGL), accompanied by the reduction of NMN$^+$ to NMNH. The NMNH produced

https://doi.org/10.1021/acscatal.2c04707
ACS Catal. 2023, 13, 1983−1998

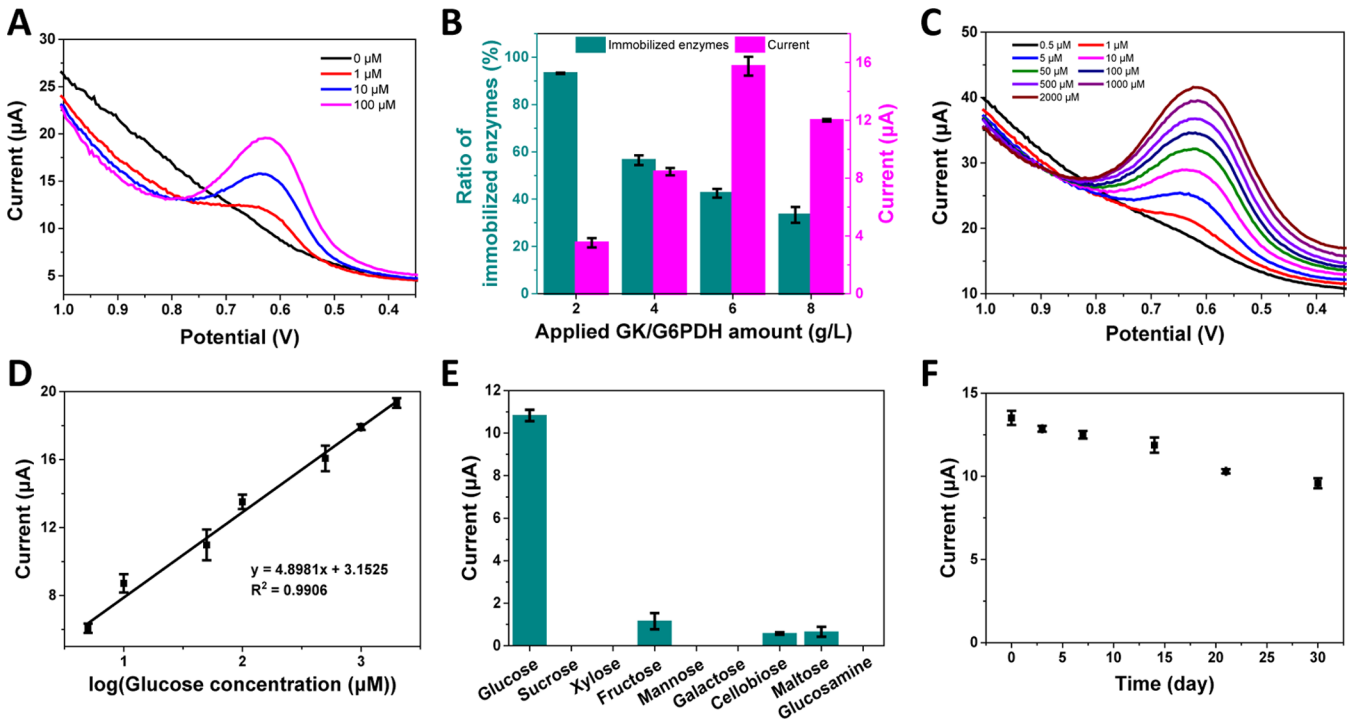

Figure 6. NMN^+-facilitated biosensor for glucose detection. (A) Differential pulse voltammetry (DPV) scanning for the GK-R4/SWCNTs/GCE under 2.0 g/L glucokinase (GK), 2.0 g/L R4, 2.0 mM NMN^+, and 5.0 mM ATP. (B) Glucokinase (GK) and ZmG6PDH R4 immobilization and current response versus the applied total GK-R4 amount from 2.0 to 8.0 mg/mL. The ratio of immobilized GK-R4 was calculated by determining the concentrations of the total added and unbound protein. The current was determined using DPV scanning under the corresponding concentration of GK-R4 and 2.0 mM NMN^+. (C) The corresponding current response of the biosensor in 0.1 M HEPES buffer (pH 7.5) with 0.5−2000 μM glucose. All measurements were performed in a 5-mL anolyte containing 2.0 mM NMN^+ and 5.0 mM ATP using a three-electrode system. (D) A typical calibration plot for glucose detection using the GK-R4/SWCNTs/GCE bioelectrode in 0.1 M HEPES buffer (pH 7.5) with various concentrations of glucose from 0.5 to 2000 μM. (E) Substrate selectivity of the bioelectrode. The assay was performed by detecting the electrocatalytic current (i_{pa}) values of 50 μM glucose or 10 mM other saccharides under 2.0 mM NMN^+ and 5.0 mM ATP. (F) Stability of the bioelectrode. After being stored at room temperature for a period, the corresponding current for 0.1 mM glucose of GK-R4/SWCNTs/GCE was investigated in a 5-mL anolyte containing 2.0 mM NMN^+ and 5.0 mM ATP using a three-electrode system. Values shown are means of triplicate determinations.

can be detected by the electrode, indicating the amount of glucose. First, SWCNTs were characterized for enzyme immobilization. Functional group-activated SWCNTs are tubular structures with a diameter of ~25 nm (Figure S14A). After binding with GK and the ZmG6PDH R4 mutant, the diameter of GK-R4/SWCNTs increased to ~35 nm with an unsmooth surface (Figure S14B). To further verify the binding between the enzymes and SWCNTs, the GK-R4 mixture was first mixed with fluorescein isothiocyanate (FITC) to form FITC-labeled GK-R4, which was then immobilized on the SWCNTs. As FITC is a fluorescent probe that emits green light upon excitation, it can be used to indicate the immobilization of enzymes on SWCNTs. As shown in Figure S14C,D, substantial green fluorescence was detected on the surface of the SWCNTs, indicating the successful construction of GK-R4/SWCNTs. The electrochemical properties of the GK-R4/SWCNT-modified glassy carbon electrode (GK-R4/SWCNTs/GCE) were investigated using DPV. There was an anodic peak of ~0.62 V in the DPV scanning for the GK-R4/SWCNTs/GCE under 2.0 g/L GK, 2.0 g/L R4, 2.0 mM NMN^+, and 5.0 mM ATP (Figure 6A). The responded electrocatalytic currents (i_{pa}) were positively correlated with glucose concentration, highlighting the excellent electron transfer properties and possible glucose detection of the GK-R4/SWCNTs/GCE.

The enzyme loading amounts of GK and R4 were subsequently optimized for improved performance of the glucose biosensor. Based on the specific activity of GK (4.0 U/mg) and R4 (0.34 U/mg) under 37 °C, the GK-R4 mixture with the same unit was obtained by mixing GK with R4 at a protein concentration ratio of 1:12. Next, a varied concentration of the GK-R4 mixture, 2.0 g/L (0.15 g/L GK and 1.85 g/L R4, corresponding to 0.6 U/mL of each enzyme) to 8.0 g/L (0.6 g/L GK and 7.4 g/L R4, corresponding to 2.4 U/mL of each enzyme), was mixed with an equal volume of 15 g/L SWCNTs, and the immobilized GK-R4 amounts and i_{pa} values were determined. As shown in Figure 6B, when the 2.0 g/L GK-R4 mixture was mixed with SWCNTs, the 1.86 g/L enzyme mixture was immobilized at an immobilized ratio of ~93%. With the increase in applied enzyme concentrations, the immobilized ratio of GK-R4 gradually decreased. When the applied enzyme amount was 8.0 g/L, ~2.7 g/L GK-R4 was immobilized, and the immobilized ratio was reduced to ~33%. While the i_{pa} values exhibited the highest response at the total enzyme loading amount of 6.0 g/L, a higher amount of GK-R4 loading largely reduced the i_{pa} value owing to the decrease of the conductivity of GK-R4/SWCNTs/GCE and thus the GK-R4 concentration of 6.0 g/L was selected for the next part of the study. Moreover, as the NMN^+ concentration increased, the i_{pa} value of the biosensor increased, and when the NMN^+ concentration exceeded 2.0 mM, the increase in the i_{pa} value

https://doi.org/10.1021/acscatal.2c04707
ACS Catal. 2023, 13, 1983−1998

was not significant (Figure S15). Next, the performance of the glucose biosensor was investigated via the DPV method by employing a three-electrode system at 37 °C in a 5-mL anolyte with 100 mM HEPES buffer (pH 7.5) containing 5.0 mM $MgCl_2$, 0.5 mM $MnCl_2$, 100 mM NaCl, 2.0 mM NMN^+, and 5.0 mM ATP. The i_{pa} value increased with the increase in glucose concentration from 5 to 2000 μM (Figure 6C), providing a positively correlated regression equation between the logarithm of glucose concentration and the current value, with a correlation coefficient of 0.9906 (Figure 6D). The detection limit of GK-R4/SWCNTs/GCE for glucose was 1 μM at a signal-to-noise (S/N) ratio of 3. The substrate selectivity of this glucose biosensor was performed by detecting the i_{pa} values of 50 μM glucose or 10 mM of other saccharides, including sucrose, xylose, fructose, mannose, galactose, cellobiose, maltose, and glucosamine (Figure 6E). In contrast to glucose, the other saccharides barely exhibited any current response, suggesting no interference with the biosensor, even at a 200-fold higher concentration of other saccharides.

After being stored at room temperature for a certain period, the corresponding i_{pa} values for 100 μM glucose of the GK-R4/SWCNTs/GCE were determined to characterize the stability of the biosensor. The current response of the biosensor remained at ∼88% and ∼71% of its initial performance after 14 and 30 days, respectively, thus indicating the high stability of this biosensor (Figure 6F). Additionally, the repeatability of this biosensor was detected using five different electrodes in a 5-mL anolyte containing 100 μM glucose, 2.0 mM NMN^+, and 5.0 mM ATP. The results showed a 9.3% relative standard deviation (RSD), indicating that the biosensor exhibited fairly good repeatability. This biosensor was used to detect glucose in two types of real samples, including fermentation broth and acid-treated corn stover-derived biomass hydrolysate.[36] The samples were filtered through a 0.22-μm membrane following centrifugation at 12,000*g* for 20 min, wherein 3.7 and 0.81 g/L glucose was detected via HPLC of fermentation broth and biomass hydrolysate, respectively. For our glucose sensor, the samples were appropriately diluted using 100 mM HEPES (pH 7.5) and added into an anolyte (100 mM HEPES buffer [pH 7.5] containing 5.0 mM $MgCl_2$, 0.5 mM $MnCl_2$, 100 mM NaCl, 2.0 mM NMN^+, and 5.0 mM ATP) to determine the respective i_{pa} values. To verify the interference of endogenous natural coenzymes in the real sample on this NMN^+-based biosensor, control reactions with 0 mM coenzyme, 2.0 mM NAD^+, and 2.0 mM $NADP^+$ were performed after the fermentation broth was diluted by 200 times. As shown in Figure S16, there was no obvious signal response in the reaction without coenzyme addition, and the signal response values were almost the same after 2.0 mM NMN^+, NAD^+, or $NADP^+$ were added into the reaction system containing diluted fermentation broth. This indicated that the accuracy of this biosensor was not affected by the presence of trace amounts of natural coenzymes and thus inexpensive and stable NMN^+ could replace the expensive and unstable natural cofactors for glucose detection. Using this biosensor, 3.2 and 0.77 g/L glucose in the fermentation broth and biomass hydrolysate samples were determined with an RSD of ∼14 and 8.5%, respectively. The recoveries of the fermentation broth and biomass hydrolysate samples were ∼87 and 95%, respectively, thereby indicating the accuracy of this biosensor in determining glucose concentration.

DISCUSSION

Enzymatic biocatalysis based on synthetic nicotinamide coenzyme biomimetics offers promising opportunities for green biomanufacturing. However, owing to the low catalytic efficiency and limited recyclability of the reduced artificial coenzymes of oxidoreductases, biomimetic coenzyme-based biocatalysis remains in its infancy.[6] Herein, *Z. mobilis* G6PDH, an important dehydrogenase for the regeneration of reduced coenzyme, was engineered from $NADP^+$-specific to $NADP^+$/NMN^+-compatible, wherein the coenzyme specificity values ($[k_{cat}/K_m]_{NMN}{}^+/[k_{cat}/K_m]_{NAD}{}^+$ and $[k_{cat}/K_m]_{NMN}{}^+/[k_{cat}/K_m]_{NADP}{}^+$) of the R4 mutant were ∼4.7 × 10^3 and 2.6 × 10^3-fold of the WT enzyme, respectively (Table 1). Although the catalytic efficiency of ZmG6PDH R4 to NMN^+ could not outperform that of WT ZmG6PDH to $NADP^+$, considering the cost of NAD^+ and NMN^+ (approximately \$2.8 × 10^3/Kg and \$1.5 × 10^3/Kg at the 100 kg scale offered by the manufacturers, respectively) and the higher stability of NMN^+ than $NAD(P)^+$,[8] using a stable, inexpensive cofactor instead of a natural and expensive cofactor is a useful strategy, particularly in the application of oxidoreductases *in vitro* at an industrial scale, similar to NMN^+-based cost-effective biomanufacturing in numerous studies.[9,22,59] Furthermore, here we revealed structural information regarding the enhanced catalytic efficiency on NMN^+ of the R4 mutant by resolving the crystal structures of apo-WT and R4:NMN^+ and performing MD simulations (Figures 2−5). Finally, a glucose biosensor with satisfactory bioelectrochemical performance was constructed based on a bioelectrode immobilized with GK and R4 ZmG6PDH, thus highlighting the prospects of the findings of this study in manufacturing glucose detection products without cryopreservation (Figure 6). Altogether, this study demonstrated a good example of linking non-natural coenzyme engineering of dehydrogenases to synthetic enzymatic biosystems, thereby providing guidance to researchers regarding the recycling of biomimetic coenzymes, oxidoreductases evolution, and developed biomimetic-based alternative tools for widespread applications.

Protein engineering to improve enzyme activity is usually implemented on the active pocket; however, pocket engineering is not omnipotent. An alternative strategy for enhancing enzyme activity on BNCs may be focusing on the overall region/domain changes, which may create convenient entry/exit or facilitate the binding of substrate/coenzyme. For example, engineering L-threonine aldolase for highly diastereoselective aldol reaction was achieved by rational molecular modification of the entrance pockets to change the substrate-binding energy.[60] Herein, the crystal structure insights and MD simulations demonstrated that positive mutants create a convenient domain interface interaction in response to the favorable binding of non-natural NMN^+, consistent with *L. mesenteroides* LmG6PDH. In the structure of LmG6PDH, the angle between the Rossmann-like and β+α domains changes with the binding of the coenzyme, forming the corresponding "open" and "closed" conformations.[55] Stabilizing the interface between these two domains of LmG6PDH might contribute to the binding of substrates or coenzymes to promote catalytic efficiency. In ZmG6PDH, when comparing the MD simulation structure of apo-R4 with the crystal structure of R4:NMN^+ and the crystal structure of apo-WT with the MD simulation structure of WT:$NADP^+$, the "open" and "closed" conformations could also be observed. Both hydrophobic and charged

https://doi.org/10.1021/acscatal.2c04707
ACS Catal. 2023, 13, 1983−1998

interactions contribute to the stability of the protein interface.[61] The M421L and S25A mutations at the surface junction of the two domains introduce more hydrophobic amino acid residues, causing closer packing between the two domains, thereby promoting the preservation of the catalytically favorable binding configuration between G6P and the smaller NMN^+ in the R4 mutant. The MD simulation results suggest that the movement of regions near the active site of ZmG6PDH R4 shift in a direction that may favor the binding of NMN^+ (Figure 5). The findings of this study show that the enzyme conformation could be modified to facilitate the binding and utilization of NMN^+, shedding light on the engineering of other oxidoreductases with a similar structure by reshaping domain interactions.

Although the mutant R4 with increased catalytic efficiency on NMN^+ was obtained and the catalytic mechanism of coenzyme recognition of R4 was analyzed, several deficiencies remain to be addressed. (1) The best mutant R4 was a $NAD(P)^+/NMN^+$-compatible dehydrogenase (Table 1). Under the coenzyme concentration of 1 mM, although the specific activity values of the optimal mutant R4 for NAD^+ and $NADP^+$ were ∼4.9 and 4.3% of the WT enzyme, respectively, these values were still much higher than those of the R4 mutant with NMN^+ as a coenzyme (Table 1). With respect to catalytic efficiency, k_{cat}/K_m of the R4 mutant on NAD^+ and $NADP^+$ were ∼21 and 226 times higher than that on NMN^+, respectively. The unsatisfied enzymatic properties of R4 cause defective NMN^+-based catalytic efficiency and serious interference of environmental natural $NAD(P)^+$. (2) The K_m value of the R4 mutant on NMN^+ is still relatively high. The K_m value of R4 on NMN^+ was 1.8×10^1 mM, which was about 49- and 307-fold of those on NAD^+ and $NADP^+$, respectively (Table 1). Therefore, a high NMN^+ concentration was required to reach its maximum reaction rate when using this BNC as a coenzyme. Similar to R4, K_m of the best mutant of *T. maritima* 6PGDH to NMN^+ was ∼14 mM,[8] which was also not conducive to biomanufacturing by enzymatic cascade catalysis. (3) With respect to structure resolution, the existing problems constitute the insufficiently high resolution of cocrystallization of R4:NMN^+, the inability to obtain the cocrystallization of R4, G6P, and NMN^+, and the lack of universal solution of oxidoreductase engineering for BNC specificity in terms of coenzymes matching and catalytic mechanism.

For further protein engineering of ZmG6PDH and other oxidoreductases for BNC recycling and the subsequent application of BNC-based biomanufacturing, several points can be considered. (1) The K_m value of R4 for NMN^+ may decrease further via protein engineering based on the crystal structure and the results of MD simulation of ZmG6PDH. An earlier study reported a BsGDH mutant with K_m of 5.9 mM[22] for NMN^+, one-third of that for ZmG6PDH R4. Although the BsGDH and ZmG6PDH R4 mutants are different in three-dimensional structures and catalytic mechanism, K_m of the R4 mutant is still high; hence, it is possible to reassess the strategy of designing the mutant library of ZmG6PDH, which includes random mutagenesis[62] and combinational multisite-saturated mutagenesis[63] to further increase the affinity of ZmG6PDH to NMN^+. Moreover, the concentration of NMN^+ in screening the positive mutants could be gradually reduced to lower K_m of ZmG6PDH mutants. In the ZmG6PDH R4 mutant, the hydrophobic mutant S115A can bind more closely with L10, L17, and L22 to form a smaller binding pocket compared with the WT enzyme, thereby increasing the binding affinity of the enzyme with the smaller coenzyme NMN^+. In addition, there exists a large space in the active pocket of the enzyme that was initially used for binding with the AMP portion of $NADP^+$. It is expected that filling this space with large side-chain groups will help enhance the enzyme activity of G6PDH against NMN^+[9,64] and maintain the channel to be large enough for NMN^+ entry simultaneously. This replacement may improve the binding affinity of ZmG6PDH to NMN^+ (reduce the K_m value) and concurrently reduce the binding affinity of ZmG6PDH to $NADP^+$ due to the increased steric hindrance, increasing catalytic efficiency under a relatively low NMN^+ loading amount in R4-mediated enzymatic biocatalysis. Moreover, by engineering the residues of *T. maritima* G6PDH that binds with the 2′-phosphate module of $NADP^+$, the TmG6PDH mutant exhibited ∼1.8 times higher specific activity on NMN^+ and a significant 62 times higher K_m for $NADP^+$ than the WT enzyme,[8] which may provide a potential implementation strategy to reduce the affinity of ZmG6PDH to natural coenzymes. Similarly, the catalytic efficiency of a 6PGDH from *T. maritima* on NMN^+ was improved by protein engineering.[8] However, the mutant 6PGDH exhibits high K_m to NMN^+, and, thus, it needs to be engineered further to decrease its K_m. Low K_m of G6PDH and 6PGDH would facilitate the biocatalysis of an enzymatic cascade based on the G6PDH-6PGDH/NMN^+ biosystem. (2) Expand the application scope of the G6PDH/6PGDH-NMN^+ biosystem. The dehydrogenase mutants (G6PDH and 6PGDH), with their enhanced activity on NMN^+, can be integrated into several *in vitro* synthetic enzymatic biosystems to produce hydrogen, bioelectricity, and high-value-added biochemicals.[8,24,26] With the boosting of our existing *in vitro* synthetic enzymatic biosystems, a successive chain of inexpensive starting substrates, such as starch, cellulose, glucose, and sucrose, can be used to facilitate the recycling of NMNH and subsequent product biosynthesis. Notably, in our previous work on xylose biosensor, the recovery of the NAD^+-dependent xylose biosensor was >125% for fermentation broth,[65] whereas in this study, the NMN^+-dependent glucose biosensor had a recovery of ∼87% for fermentation broth, which may be attributed to the trace amount of natural coenzyme following the dilution of the detected sample for hundreds of times or the biorthogonality of this NMN^+-dependent enzymatic process. In any case, G6PDH and 6PGDH with high activity on NMN^+ and little activity on natural cofactors provide a promising opportunity for establishing biorthogonal systems, which can address this complex problem to generate a pathway-specific driving force in synthetic biology and analyze the metabolic network in systems biology.[66]

In summary, a $NADP^+/NMN^+$-compatible mutant (R4) of ZmG6PDH was obtained via protein engineering based on a validated plate-dependent high-throughput screening method. Compared with the WT ZmG6PDH, the R4 mutant exhibited $\sim 4.7 \times 10^3$ and 2.6×10^3-fold of the two coenzyme specificity values ($[k_{cat}/K_m]_{NMN^+}/[k_{cat}/K_m]_{NAD^+}$ and $[k_{cat}/K_m]_{NMN^+}/[k_{cat}/K_m]_{NADP^+}$), respectively. Based on the structural information and results of the MD simulations, the helix region of the mutant R4 moves closer to the active site, creating a convenient interface interaction between the two domains of mutant R4 that may favor the binding of NMN^+. Additionally, we have demonstrated the application of the G6PDH-NMN^+ biosystem for a glucose biosensor with an acceptable bioelectrochemical performance without cryopreservation. Collectively, the accessibility of this G6PDH-NMN^+ biosystem

https://doi.org/10.1021/acscatal.2c04707
ACS Catal. 2023, 13, 1983−1998

should provide unique tools and research guidelines for the effective regeneration of reduced synthetic BNCs, further expanding the scope of these artificial biosystems for *in vitro* and *in vivo* applications.

■ ASSOCIATED CONTENT

Supporting Information

The Supporting Information is available free of charge at https://pubs.acs.org/doi/10.1021/acscatal.2c04707.

Additional material pertaining to experimental results (Figures S1−S16, Tables S1−S3) (PDF)

■ AUTHOR INFORMATION

Corresponding Authors

Hao Su − *Tianjin Institute of Industrial Biotechnology, Chinese Academy of Sciences, Tianjin 300308, People's Republic of China; National Center of Technology Innovation for Synthetic Biology, Tianjin 300308, People's Republic of China;* orcid.org/0000-0002-0178-6610; Email: suhao@tib.cas.cn

Chun You − *Tianjin Institute of Industrial Biotechnology, Chinese Academy of Sciences, Tianjin 300308, People's Republic of China; University of Chinese Academy of Sciences, Beijing 100049, People's Republic of China; National Center of Technology Innovation for Synthetic Biology, Tianjin 300308, People's Republic of China;* orcid.org/0000-0003-2305-336X; Email: you_c@tib.cas.cn

Authors

Dongdong Meng − *Tianjin Institute of Industrial Biotechnology, Chinese Academy of Sciences, Tianjin 300308, People's Republic of China;* orcid.org/0000-0001-9913-1016

Meixia Liu − *Tianjin Institute of Industrial Biotechnology, Chinese Academy of Sciences, Tianjin 300308, People's Republic of China; University of Chinese Academy of Sciences, Beijing 100049, People's Republic of China;* orcid.org/0000-0002-2580-3841

Haiyan Song − *Tianjin Institute of Industrial Biotechnology, Chinese Academy of Sciences, Tianjin 300308, People's Republic of China*

Lijie Chen − *Tianjin Institute of Industrial Biotechnology, Chinese Academy of Sciences, Tianjin 300308, People's Republic of China; Key Laboratory of Industrial Fermentation Microbiology, Ministry of Education, College of Bioengineering, Tianjin University of Science and Technology, Tianjin 300453, People's Republic of China*

Qiangzi Li − *Tianjin Institute of Industrial Biotechnology, Chinese Academy of Sciences, Tianjin 300308, People's Republic of China; University of Chinese Academy of Sciences, Beijing 100049, People's Republic of China*

Ya-nan Liu − *Tianjin Institute of Industrial Biotechnology, Chinese Academy of Sciences, Tianjin 300308, People's Republic of China*

Zhiguang Zhu − *Tianjin Institute of Industrial Biotechnology, Chinese Academy of Sciences, Tianjin 300308, People's Republic of China;* orcid.org/0000-0002-6625-5087

Weidong Liu − *Tianjin Institute of Industrial Biotechnology, Chinese Academy of Sciences, Tianjin 300308, People's Republic of China;* orcid.org/0000-0001-7954-7700

Xiang Sheng − *Tianjin Institute of Industrial Biotechnology, Chinese Academy of Sciences, Tianjin 300308, People's Republic of China; University of Chinese Academy of Sciences, Beijing 100049, People's Republic of China; National Center of Technology Innovation for Synthetic Biology, Tianjin 300308, People's Republic of China;* orcid.org/0000-0002-6542-6649

Yi-Heng P. Job Zhang − *Tianjin Institute of Industrial Biotechnology, Chinese Academy of Sciences, Tianjin 300308, People's Republic of China; in vitro Synthetic Biology Center, Tianjin Institute of Industrial Biotechnology, Chinese Academy of Sciences, Tianjin 300308, People's Republic of China*

Complete contact information is available at: https://pubs.acs.org/10.1021/acscatal.2c04707

Author Contributions

#D.M. and M.L. contributed equally to this work. Y.-H.P.J.Z. proposed the idea of enhancing the catalytic efficiency on NMN^+ of G6PDH. C.Y. and D.M. designed the experiments. D.M. performed enzyme engineering, enzymatic characteristic, and electrochemical experiments. M.L. and W.L. conducted protein crystallization and structure determination experiments. H.S. (Hao Su) and X.S. conducted the molecular dynamics simulation. H.S. (Haiyan Song) and Z.Z. provided guidance in electrochemical experiments. D.M., M.L., H.S. (Hao Su), X.S., Y.-H.P.J.Z., and C.Y. analyzed the data and drafted the manuscript. All authors discussed the results and commented on the manuscript.

Notes

The authors declare the following competing financial interest(s): Chun You and Dongdong Meng are the co-inventors of the ZmG6PDH mutants that could utilize NMN+ as the coenzyme, and these mutants are covered under a Chinese patent (CN 113046335 A).

■ ACKNOWLEDGMENTS

This work was supported by the National Natural Science Foundation of China (Grant No. 32022044 and 21778073), the National Key Research and Development Program of China (2021YFC2102300), and the Tianjin Synthetic Biotechnology Innovation Capacity Improvement Project (Grant No. TSBICIP-KJGG-003 and TSBICIP-CXRC-063).

■ REFERENCES

(1) Chen, K.; Arnold, F. H. Engineering new catalytic activities in enzymes. *Nat. Catal.* **2020**, *3*, 203−213.

(2) You, Z.-N.; Chen, Q.; Shi, S.-C.; Zheng, M.-M.; Pan, J.; Qian, X.-L.; Li, C.-X.; Xu, J.-H. Switching cofactor dependence of 7β-hydroxysteroid dehydrogenase for cost-effective production of ursodeoxycholic acid. *ACS Catal.* **2019**, *9*, 466−473.

(3) Zhang, J. D.; Yang, X. X.; Jia, Q.; Zhao, J. W.; Gao, L. L.; Gao, W. C.; Chang, H. H.; Wei, W. L.; Xu, J. H. Asymmetric ring opening of racemic epoxides for enantioselective synthesis of (S)-amino alcohols by a cofactor self-sufficient cascade biocatalysis system. *Catal. Sci. Technol.* **2019**, *9*, 70−74.

(4) Paul, C. E.; Hollmann, F. A survey of synthetic nicotinamide cofactors in enzymatic processes. *Appl. Microbiol. Biotechnol.* **2016**, *100*, 4773−4778.

(5) You, C.; Huang, R.; Wei, X.; Zhu, Z.; Zhang, Y. P. Protein engineering of oxidoreductases utilizing nicotinamide-based coenzymes, with applications in synthetic biology. *Synth. Syst. Biotechnol.* **2017**, *2*, 208−218.

(6) Zachos, I.; Nowak, C.; Sieber, V. Biomimetic cofactors and methods for their recycling. *Curr. Opin. Chem. Biol.* **2019**, *49*, 59−66.
(7) King, E.; Maxel, S.; Li, H. Engineering natural and noncanonical nicotinamide cofactor-dependent enzymes: design principles and technology development. *Curr. Opin. Biotechnol.* **2020**, *66*, 217−226.
(8) Huang, R.; Chen, H.; Upp, D. M.; Lewis, J. C.; Job Zhang, Y. P. A high-throughput method for directed evolution of $NAD(P)^+$-dependent dehydrogenases for the reduction of biomimetic nicotinamide analogues. *ACS Catal.* **2019**, *9*, 11709−11719.
(9) Zhang, L.; King, E.; Black, W. B.; Heckmann, C. M.; Wolder, A.; Cui, Y.; Nicklen, F.; Siegel, J. B.; Luo, R.; Paul, C. E.; Li, H. Directed evolution of phosphite dehydrogenase to cycle noncanonical redox cofactors via universal growth selection platform. *Nat. Commun.* **2022**, *13*, No. 5021.
(10) Löw, S. A.; Low, I. M.; Weissenborn, M. J.; Hauer, B. Enhanced ene-reductase activity through alteration of artificial nicotinamide cofactor substituents. *ChemCatChem* **2016**, *8*, 911−915.
(11) Knaus, T.; Paul, C. E.; Levy, C. W.; de Vries, S.; Mutti, F. G.; Hollmann, F.; Scrutton, N. S. Better than nature: Nicotinamide biomimetics that outperform natural coenzymes. *J. Am. Chem. Soc.* **2016**, *138*, 1033−1039.
(12) Paul, C. E.; Gargiulo, S.; Opperman, D. J.; Lavandera, I.; Gotor-Fernandez, V.; Gotor, V.; Taglieber, A.; Arends, I. W.; Hollmann, F. Mimicking nature: Synthetic nicotinamide cofactors for C=C bioreduction using enoate reductases. *Org. Lett.* **2013**, *15*, 180−183.
(13) Friedlos, F.; Jarman, M.; Davies, L. C.; Boland, M. P.; Knox, R. J. Identification of novel reduced pyridinium derivatives as synthetic cofactors for the enzyme DT diaphorase (NAD(P)H dehydrogenase (quinone), EC 1.6.99.2). *Biochem. Pharmacol.* **1992**, *44*, 25−31.
(14) Zhang, L.; Yuan, J.; Xu, Y. F.; Zhang, Y. H. P.; Qian, X. H. New artificial fluoro-cofactor of hydride transfer with novel fluorescence assay for redox biocatalysis. *Chem. Commun.* **2016**, *52*, 6471−6474.
(15) Knox, R. J.; Friedlos, F.; Jarman, M.; Davies, L. C.; Goddard, P.; Anlezark, G. M.; Melton, R. G.; Sherwood, R. F. Virtual cofactors for an *Escherichia coli* nitroreductase enzyme: Relevance to reductively activated prodrugs in antibody-directed enzyme prodrug therapy (ADEPT). *Biochem. Pharmacol.* **1995**, *49*, 1641−1647.
(16) Paul, C. E.; Tischler, D.; Riedel, A.; Heine, T.; Itoh, N.; Hollmann, F. Nonenzymatic regeneration of styrene monooxygenase for catalysis. *ACS Catal.* **2015**, *5*, 2961−2965.
(17) Nowak, C.; Beer, B.; Pick, A.; Roth, T.; Lommes, P.; Sieber, V. A water-forming NADH oxidase from *Lactobacillus pentosus* suitable for the regeneration of synthetic biomimetic cofactors. *Front. Microbiol.* **2015**, *6*, 957.
(18) Nowak, C.; Pick, A.; Csepei, L. I.; Sieber, V. Characterization of biomimetic cofactors according to stability, redox potentials, and enzymatic conversion by NADH oxidase from *Lactobacillus pentosus*. *ChemBioChem* **2017**, *18*, 1944−1949.
(19) Weusthuis, R. A.; Folch, P. L.; Pozo-Rodriguez, A.; Paul, C. E. Applying non-canonical redox cofactors in fermentation processes. *iScience* **2020**, *23*, 101471.
(20) Campbell, E.; Meredith, M.; Minteer, S. D.; Banta, S. Enzymatic biofuel cells utilizing a biomimetic cofactor. *Chem. Commun.* **2012**, *48*, 1898−1900.
(21) Nowak, C.; Pick, A.; Lommes, P.; Sieber, V. Enzymatic reduction of nicotinamide biomimetic cofactors using an engineered glucose dehydrogenase: Providing a regeneration system for artificial cofactors. *ACS Catal.* **2017**, *7*, 5202−5208.
(22) Black, W. B.; Zhang, L.; Mak, W. S.; Maxel, S.; Cui, Y.; King, E.; Fong, B.; Sanchez Martinez, A.; Siegel, J. B.; Li, H. Engineering a nicotinamide mononucleotide redox cofactor system for biocatalysis. *Nat. Chem. Biol.* **2020**, *16*, 87−94.
(23) Zachos, I.; Genth, R.; Sutiono, S.; Marczynski, M.; Lieleg, O.; Sieber, V. Hot flows: Evolving an archaeal glucose dehydrogenase for ultrastable carba-$NADP^+$ using microfluidics at elevated temperatures. *ACS Catal.* **2022**, *12*, 1841−1846.
(24) Zhu, Z.; Zhang, Y.-H. P. In vitro metabolic engineering of bioelectricity generation by the complete oxidation of glucose. *Metab. Eng.* **2017**, *39*, 110−116.
(25) Zhu, Z.; Kin Tam, T.; Sun, F.; You, C.; Zhang, Y.-H. P. A high-energy-density sugar biobattery based on a synthetic enzymatic pathway. *Nat. Commun.* **2014**, *5*, No. 3026.
(26) Kim, E. J.; Kim, J. E.; Zhang, Y. H. P. J. Ultra-rapid rates of water splitting for biohydrogen gas production through in vitro artificial enzymatic pathways. *Energy Environ. Sci.* **2018**, *11*, 2064−2072.
(27) Rollin, J. A.; Martin del Campo, J.; Myung, S.; Sun, F.; You, C.; Bakovic, A.; Castro, R.; Chandrayan, S. K.; Wu, C. H.; Adams, M. W.; Senger, R. S.; Zhang, Y.-H. P. High-yield hydrogen production from biomass by in vitro metabolic engineering: Mixed sugars coutilization and kinetic modeling. *Proc. Natl. Acad. Sci. U.S.A.* **2015**, *112*, 4964−4969.
(28) Su, H. H.; Guo, Z. W.; Wu, X. L.; Xu, P.; Li, N.; Zong, M. H.; Lou, W. Y. Efficient bioconversion of sucrose to high-value-added glucaric acid by in vitro metabolic engineering. *ChemSusChem* **2019**, *12*, 2278−2285.
(29) Ogawa, Z.; Kanashima, M.; Nishioka, H. Improvement of the quantitative method for glucose determination using hexokinase and glucose 6-phosphate dehydrogenase. *Clin. Chem. Lab. Med.* **2001**, *39*, 396−400.
(30) Srivastava, P. K.; Singh, S. Immobilization and applications of glucose-6-phosphate dehydrogenase: A review. *Prep. Biochem. Biotechnol.* **2013**, *43*, 376−384.
(31) Sahin, S.; Ozmen, I.; Bastemur, G. Y.; Ozkorucuklu, S. P. Development of voltammetric glucose-6-phosphate biosensors based on the immobilization of glucose-6-phosphate dehydrogenase on polypyrrole- and chitosan-coated Fe_3O_4 nanoparticles/polypyrrole nanocomposite films. *Appl. Biochem. Biotechnol.* **2019**, *188*, 1145−1157.
(32) Hansen, T.; Schonheit, P. ATP-dependent glucokinase from the hyperthermophilic bacterium *Thermotoga maritima* represents an extremely thermophilic ROK glucokinase with high substrate specificity. *FEMS Microbiol. Lett.* **2003**, *226*, 405−411.
(33) Huang, R.; Chen, H.; Zhou, W.; Ma, C.; Zhang, Y. P. Engineering a thermostable highly active glucose 6-phosphate dehydrogenase and its application to hydrogen production in vitro. *Appl. Microbiol. Biotechnol.* **2018**, *102*, 3203−3215.
(34) Zhu, Z.; Sun, F.; Zhang, X.; Zhang, Y. H. Deep oxidation of glucose in enzymatic fuel cells through a synthetic enzymatic pathway containing a cascade of two thermostable dehydrogenases. *Biosens. Bioelectron.* **2012**, *36*, 110−115.
(35) Kanji, M. I.; Toews, M. L.; Carper, W. R. A kinetic study of glucose-6-phosphate dehydrogenase. *J. Biol. Chem.* **1976**, *251*, 2258−2262.
(36) Meng, D.; Wei, X.; Zhang, Y.-H. P. J.; Zhu, Z.; You, C.; Ma, Y. Stoichiometric conversion of cellulosic biomass by in vitro synthetic enzymatic biosystems for biomanufacturing. *ACS Catal.* **2018**, *8*, 9550−9559.
(37) Minor, W.; Cymborowski, M.; Otwinowski, Z.; Chruszcz, M. HKL-3000: The integration of data reduction and structure solution from diffraction images to an initial model in minutes. *Acta Crystallogr. Sect. D Biol. Crystallogr.* **2006**, *62*, 859−866.
(38) Karplus, P. A.; Diederichs, K. Assessing and maximizing data quality in macromolecular crystallography. *Curr. Opin. Struct. Biol.* **2015**, *34*, 60−68.
(39) Winn, M. D.; Ballard, C. C.; Cowtan, K. D.; Dodson, E. J.; Emsley, P.; Evans, P. R.; Keegan, R. M.; Krissinel, E. B.; Leslie, A. G.; McCoy, A.; McNicholas, S. J.; Murshudov, G. N.; Pannu, N. S.; Potterton, E. A.; Powell, H. R.; Read, R. J.; Vagin, A.; Wilson, K. S. Overview of the CCP4 suite and current developments. *Acta Crystallogr. Sect. D: Biol. Crystallogr.* **2011**, *67*, 235−242.
(40) Emsley, P.; Cowtan, K. Coot: model-building tools for molecular graphics. *Acta Crystallogr. Sect. D: Biol. Crystallogr.* **2004**, *60*, 2126−2132.
(41) Adams, P. D.; Grosse-Kunstleve, R. W.; Hung, L. W.; Ioerger, T. R.; McCoy, A. J.; Moriarty, N. W.; Read, R. J.; Sacchettini, J. C.; Sauter, N. K.; Terwilliger, T. C. PHENIX: Building new software for

https://doi.org/10.1021/acscatal.2c04707
ACS Catal. 2023, 13, 1983−1998

automated crystallographic structure determination. *Acta Crystallogr. Sect. D: Biol. Crystallogr.* **2002**, *58*, 1948−1954.
(42) Mercaldi, G. F.; Dawson, A.; Hunter, W. N.; Cordeiro, A. T. The structure of a *Trypanosoma cruzi* glucose-6-phosphate dehydrogenase reveals differences from the mammalian enzyme. *FEBS Lett.* **2016**, *590*, 2776−2786.
(43) Duan, Y.; Wu, C.; Chowdhury, S.; Lee, M. C.; Xiong, G.; Zhang, W.; Yang, R.; Cieplak, P.; Luo, R.; Lee, T.; Caldwell, J.; Wang, J.; Kollman, P. A point-charge force field for molecular mechanics simulations of proteins based on condensed-phase quantum mechanical calculations. *J. Comput. Chem.* **2003**, *24*, 1999−2012.
(44) Cornell, W. D.; Cieplak, P.; Bayly, C. I.; Gould, I. R.; Merz, K. M.; Ferguson, D. M.; Spellmeyer, D. C.; Fox, T.; Caldwell, J. W.; Kollman, P. A. A second generation force field for the simulation of proteins, nucleic acids, and organic molecules. *J. Am. Chem. Soc.* **1995**, *117*, 5179−5197.
(45) Wang, J.; Wolf, R. M.; Caldwell, J. W.; Kollman, P. A.; Case, D. A. Development and testing of a general amber force field. *J. Comput. Chem.* **2004**, *25*, 1157−1174.
(46) Bayly, C. I.; Cieplak, P.; Cornell, W.; Kollman, P. A. A well-behaved electrostatic potential based method using charge restraints for deriving atomic charges: The RESP model. *J. Phys. Chem. A* **1993**, *97*, 10269−10280.
(47) Cornell, W. D.; Cieplak, P.; Bayly, C. I.; Kollman, P. A. Application of RESP charges to calculate conformational energies, hydrogen bond energies, and free energies of solvation. *J. Am. Chem. Soc.* **1993**, *115*, 9620−9631.
(48) Case, D. A.; Ben-Shalom, I. Y.; Brozell, S. R.; Cerutti, D. S.; Cheatham, T. E.; Cruzeiro, V. W. D.; Darden, T. A.; Duke, R. E.; Ghoreishi, D.; Gilson, M. K.; Gohlke, H.; Goetz, A. W.; Greene, D.; Harris, R.; Homeyer, N.; Huang, Y.; Izadi, S.; Kovalenko, A.; Kurtzman, T.; Lee, T. S.; LeGrand, S.; Li, P.; Lin, C.; Liu, J.; Luchko, T.; Luo, R.; Mermelstein, D. J.; Merz, K. M.; Miao, Y.; Monard, G.; Nguyen, C.; Nguyen, H.; Omelyan, I.; Onufriev, A.; Pan, F.; Qi, R.; Roe, D. R.; Roitberg, A.; Sagui, C.; Schott-Verdugo, S.; Shen, J.; Simmerling, C. L.; Smith, J.; SalomonFerrer, R.; Swails, J.; Walker, R. C.; Wang, J.; Wei, H.; Wolf, R. M.; Wu, X.; Xiao, L.; York, D. M.; Kollman, P. A.. *AMBER 2018*. University of California: San Francisco, 2018.
(49) Jorgensen, W. L.; Chandrasekhar, J.; Madura, J. D.; et al. Comparison of simple potential functions for simulating liquid water. *J. Chem. Phys.* **1983**, *79*, 926−935.
(50) Ryckaert, J.-P.; Ciccotti, G.; Berendsen, H. J. C. Numerical integration of the cartesian equations of motion of a system with constraints: molecular dynamics of *n*-alkanes. *J. Comput. Phys.* **1977**, *23*, 327−341.
(51) Darden, T.; York, D.; Pedersen, L. Particle mesh Ewald: An N·log(*N*) method for Ewald sums in large systems. *J. Chem. Phys.* **1993**, *98*, 10089.
(52) Roe, D. R.; Cheatham, T. E., 3rd PTRAJ and CPPTRAJ: Software for processing and analysis of molecular dynamics trajectory data. *J. Chem. Theory Comput.* **2013**, *9*, 3084−3095.
(53) Cao, G.; Gao, J.; Zhou, L.; Huang, Z.; He, Y.; Zhu, M.; Jiang, Y. Fabrication of Ni^{2+} -nitrilotriacetic acid functionalized magnetic mesoporous silica nanoflowers for one pot purification and immobilization of His-tagged *ω*-transaminase. *Biochem. Eng. J.* **2017**, *128*, 116−125.
(54) Xu, W.; Jiao, L.; Yan, H.; Wu, Y.; Chen, L.; Gu, W.; Du, D.; Lin, Y.; Zhu, C. Glucose oxidase-integrated metal-organic framework hybrids as biomimetic cascade nanozymes for ultrasensitive glucose biosensing. *ACS Appl. Mater. Interfaces* **2019**, *11*, 22096−22101.
(55) Naylor, C. E.; Gover, S.; Basak, A. K.; Cosgrove, M. S.; Levy, H. R.; Adams, M. J. $NADP^+$ and NAD^+ binding to the dual coenzyme specific enzyme *Leuconostoc mesenteroides* glucose 6-phosphate dehydrogenase: different interdomain hinge angles are seen in different binary and ternary complexes. *Acta Crystallogr. Sect. D: Biol. Crystallogr.* **2001**, *57*, 635−648.
(56) Perálvarez-Marín, A.; Lorenz-Fonfria, V. A.; Simon-Vazquez, R.; Gomariz, M.; Meseguer, I.; Querol, E.; Padros, E. Influence of proline on the thermostability of the active site and membrane arrangement of transmembrane proteins. *Biophys. J.* **2008**, *95*, 4384−4395.
(57) Dotsenko, A. S.; Pramanik, S.; Gusakov, A. V.; Rozhkova, A. M.; Zorov, I. N.; Sinitsyn, A. P.; Davari, M. D.; Schwaneberg, U. Critical effect of proline on thermostability of endoglucanase II from *Penicillium verruculosum*. *Biochem. Eng. J.* **2019**, *152*, No. 107395.
(58) Rose, G. D.; Geselowitz, A. R.; Lesser, G. J.; Lee, R. H.; Zehfus, M. H. Hydrophobicity of amino acid residues in globular proteins. *Science* **1985**, *229*, 834−838.
(59) Richardson, K. N.; Black, W. B.; Li, H. Aldehyde production in crude lysate- and whole cell-based biotransformation using a noncanonical redox cofactor system. *ACS Catal.* **2020**, *10*, 8898−8903.
(60) Zheng, W.; Chen, K.; Wang, Z.; Cheng, X.; Xu, G.; Lirong, Yang.; Wu, J. Construction of a highly diastereoselective aldol reaction system with L-threonine aldolase by computer-assisted rational molecular modification and medium engineering. *Org. Lett.* **2020**, *22*, 5763−5767.
(61) Brinda, K. V.; Kannan, N.; Vishveshwara, S. Analysis of homodimeric protein interfaces by graph-spectral methods. *Protein Eng.* **2002**, *15*, 265−277.
(62) Chen, K.; Arnold, F. H. Tuning the activity of an enzyme for unusual environments: sequential random mutagenesis of subtilisin E for catalysis in dimethylformamide. *Proc. Natl. Acad. Sci. U.S.A.* **1993**, *90*, 5618−5622.
(63) Wang, J.; Guo, X.; Wan, L.; Liu, Y.; Xue, H.; Zhao, Z. K. Engineering formaldehyde dehydrogenase from pseudomonas putida to favor nicotinamide cytosine dinucleotide. *ChemBioChem* **2022**, *23*, No. e202100697.
(64) Liu, Y.; Feng, Y.; Wang, L.; Guo, X.; Liu, W.; Li, Q.; Wang, X.; Xue, S.; Zhao, Z. K. Structural insights into phosphite dehydrogenase variants favoring a non-natural redox cofactor. *ACS Catal.* **2019**, *9*, 1883−1887.
(65) Song, H.; Gao, G.; Ma, C.; Li, Y.; Shi, J.; Zhou, X.; Zhu, Z. A hybrid system integrating xylose dehydrogenase and NAD^+ coupled with PtNPs@MWCNTs composite for the real-time biosensing of xylose. *Analyst* **2020**, *145*, 5563−5570.
(66) Wang, X.; Feng, Y.; Guo, X.; Wang, Q.; Ning, S.; Li, Q.; Wang, J.; Wang, L.; Zhao, Z. K. Creating enzymes and self-sufficient cells for biosynthesis of the non-natural cofactor nicotinamide cytosine dinucleotide. *Nat. Commun.* **2021**, *12*, No. 2116.

https://doi.org/10.1021/acscatal.2c04707
ACS Catal. 2023, 13, 1983−1998